

CONSTRAINTS ON COSMOLOGY AND BARYONIC FEEDBACK WITH THE DEEP LENS SURVEY USING GALAXY-GALAXY AND GALAXY-MASS POWER SPECTRA

MIJIN YOON¹, M. JAMES JEE^{1,2},
J. ANTHONY TYSON², SAMUEL SCHMIDT², DAVID WITTMAN², AND AMI CHOI³

Draft version May 29, 2022

ABSTRACT

We present cosmological parameter measurements from the Deep Lens Survey (DLS) using galaxy-mass and galaxy-galaxy power spectra in the multipole range $\ell = 250 \sim 2000$. We measure galaxy-galaxy power spectra from two lens bins centered at $z \sim 0.27$ and 0.54 and galaxy-mass power spectra by cross-correlating the positions of galaxies in these two lens bins with galaxy shapes in two source bins centered at $z \sim 0.64$ and 1.1 . We marginalize over a baryonic feedback process using a single-parameter representation and a sum of neutrino masses, as well as photometric redshift and shear calibration systematic uncertainties. For a flat Λ CDM cosmology, we determine $S_8 \equiv \sigma_8 \sqrt{\Omega_m}/0.3 = 0.818_{-0.039}^{+0.031}$, in good agreement with our previous DLS cosmic shear and the Planck Cosmic Microwave Background (CMB) measurements. Without the baryonic feedback marginalization, S_8 decreases by ~ 0.05 because the dark matter-only power spectrum lacks the suppression at the highest ℓ 's due to Active Galactic Nuclei (AGN) feedback processes. Together with the Planck CMB measurement, we constrain the baryonic feedback parameter to $A_{\text{baryon}} = 1.07_{-0.37}^{+0.29}$, which suggests an interesting possibility that the actual AGN feedback might be stronger than the recipe used in the OWLS simulations. The interpretation is limited by the validity of this one-parameter representation of the baryonic feedback effect.

Keywords: cosmological parameters — gravitational lensing: weak — dark matter — cosmology: observations — large-scale structure of Universe

1. INTRODUCTION

The initial conditions of our universe leave distinctive footprints on both the large scale structure and the cosmic expansion history. To determine these conditions (or more commonly referred to as cosmological parameters), a number of efforts have been made in the past few decades (e.g., Bennett et al. 2003; Eisenstein et al. 2005; Allen et al. 2011; Suzuki et al. 2012; Hildebrandt et al. 2017) and similar projects on more massive scales will begin their operations in the current decade [e.g., Large Synoptic Survey Telescope (LSST)⁴; Wide-Field Infrared Survey Telescope (W-FIRST)⁵; Euclid⁶; Square Kilometer Array (SKA)⁷; eROSITA⁸] through various observations including the cosmic microwave background (CMB), Type Ia supernovae, baryonic acoustic oscillations (BAO), galaxy clusters, and clustering properties of galaxies and dark matter.

Studying clustering properties of galaxies and dark matter with weak lensing is among the most powerful methods among the aforementioned observations. The weak-lensing signal is sensitive to both geometric and clustering properties of the universe. Past weak-lensing

efforts have focused on measuring the clustering properties of the total mass (e.g., Kitching et al. 2007; Schrabback et al. 2010; Heymans et al. 2012; Jee et al. 2013; Huff et al. 2014; Hildebrandt et al. 2017). This so-called “cosmic shear” measures shape correlations of distant galaxies to infer clustering properties of foreground total matter (dark matter + baryonic matter) without utilizing the information provided by galaxies, the visible components of the foreground structure. The reason that the clustering properties of galaxies alone have not been used for precision cosmology is that galaxies are biased tracers of foreground structures. However, it has been suggested that this bias can be effectively constrained by combining galaxy auto-correlation and galaxy-mass correlation data (e.g., Zhan 2006; Cacciato et al. 2013; Mandelbaum et al. 2013; Kwan et al. 2017; Abbott et al. 2017; van Uitert et al. 2018). The combination enables cosmological parameter constraints because we can determine both the matter power spectrum P_δ and the galaxy bias b via the relations $P^{gm} \propto bP_\delta$ and $P^{gg} \propto b^2P_\delta$, where P^{gm} and P^{gg} are the galaxy-mass and galaxy-galaxy power spectra. Hereafter, we will refer to this method based on the combined analysis of galaxy-galaxy and galaxy-mass correlations as G³M for brevity; sometimes, the probe from the combination of all three two-point correlations (i.e., galaxy-galaxy, galaxy-mass, and mass-mass) is termed the “3 × 2pt” method.

It is useful to probe the matter power spectrum of our universe through both cosmic shear and G³M for the following reasons. First, as demonstrated by previous studies, the constraints from the G³M method are nearly independent of those from cosmic shear even if the signals are extracted from the same survey data. Second, the

¹ Department of Astronomy, Yonsei University, Yonsei-ro 50, Seoul, Korea; mjyoon@yonsei.ac.kr, mkjee@yonsei.ac.kr

² Department of Physics, University of California, Davis, California, USA

³ Center for Cosmology and AstroParticle Physics, The Ohio State University, 191 West Woodruff Avenue, Columbus, OH 43210, USA

⁴ <http://www.lsst.org>

⁵ <https://wfirst.gsfc.nasa.gov>

⁶ <http://sci.esa.int/euclid>

⁷ <https://www.skatelescope.org>

⁸ <http://www.mpe.mpg.de/eROSITA>

two methods have different sensitivities to weak-lensing systematics. For example, the so-called additive shear bias tends to be cancelled in G^3M as tangential shears are azimuthally averaged around lens galaxies. On the other hand, in cosmic shear additive shear bias modulates the shear-shear correlation amplitude non-negligibly. Also, intrinsic alignments have much smaller impacts on the G^3M signals, where they become important only when a galaxy that is physically close to a lens is mistaken for a source by photometric redshift errors. However, in cosmic shear the shear-intrinsic ellipticity correlations (so-called GI systematics) affect the shear correlation between two galaxies separated by a large redshift difference. Therefore, comparison of cosmological parameter constraints between the two methods provides critical insights on both instrumental and astrophysical systematics.

In this paper, we present cosmological parameter measurements from the Deep Lens Survey (DLS) by combining galaxy-mass and galaxy-galaxy power spectra. This is the third paper of the cosmology series from the DLS. In our two previous studies (Jee et al. 2013, 2016), we studied cosmology using two-dimensional (projected) and three-dimensional (tomographic) cosmic shear analyses. The previous DLS results are interesting in several aspects. First, despite the small survey area, the constraining power of the DLS is comparable or greater than those of other larger ($> 100 \text{ deg}^2$) surveys thanks to its depth. Second, the results provide no tension with the Planck cosmological parameters based on CMB measurements (Planck Collaboration et al. 2016, hereafter Planck2015) while some recent weak-lensing results can be interpreted as indicating $> 2\sigma$ tensions (e.g., MacCrann et al. 2015; Leauthaud et al. 2017). If ultimately found to be statistically significant, the discrepancy might be a serious challenge to the current Λ CDM paradigm. However, the conclusion should await scrutiny of all possible systematics. Occasionally, different analysis methods lead to non-negligible differences even for the same data (e.g., Chang et al. 2018 in preparation). Certainly, this is one of the motivations of the current DLS study based on the G^3M method. Additionally, in the current study we address the baryonic feedback effect using the power spectrum of Mead et al. (2015), which models the power suppression on small scales due to AGN feedback. Therefore, the results from the current study serve as interesting comparisons to our previous cosmic shear-based results and also provide invaluable opportunity to reveal hidden systematics if the results are found to be statistically discrepant.

Our paper is structured as follows. We present the theoretical background in §2. The DLS data and signal constructions are described in §3. Our main cosmological parameter constraining results and discussions are presented in §4 and §5, respectively before the conclusion in §6. In Figure 1, we summarize the flow of our analysis of the DLS data to constrain cosmological parameters from galaxy-galaxy lensing and galaxy clustering measurements.

2. THEORETICAL BACKGROUND

In the current study, we use power spectrum estimators to constrain cosmological parameters. The power spectrum estimators were first suggested in Schneider

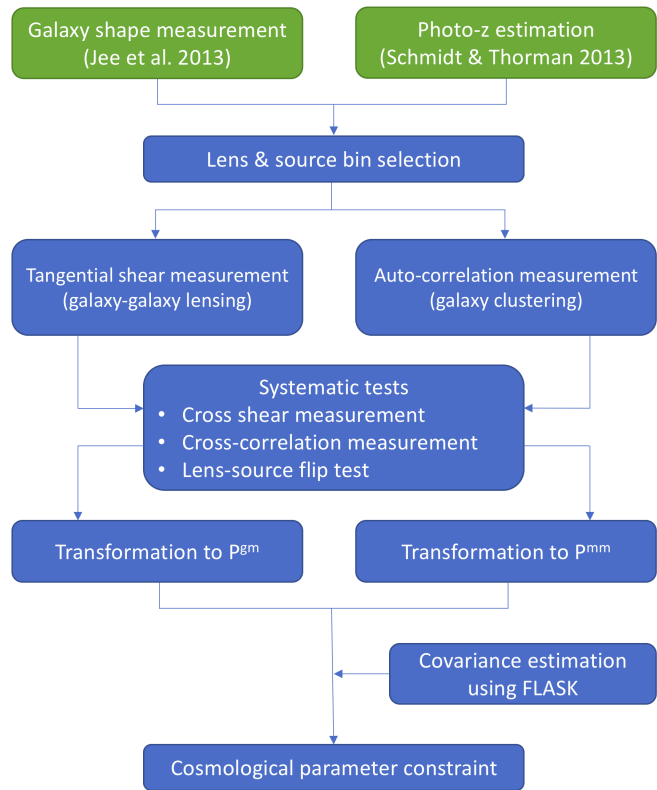


Figure 1. Flowchart of our cosmological parameter constraints using galaxy-galaxy lensing and galaxy clustering signals from the DLS.

et al. (2002). Among recent studies using combined analysis of galaxy-galaxy lensing and galaxy clustering, Köhlinger et al. (2016, 2017) and van Uitert et al. (2018) utilize power spectrum estimators, which have the following advantages. The power spectrum estimators are more fundamental than real space estimators because they are more directly related to the matter power spectrum whereas the correlation functions are obtained after convolving these galaxy-galaxy/galaxy-mass power spectrum with highly oscillatory kernels. Thus, if separation of small scales from large scales is clear in the matter power spectrum, in principle cosmological studies with power spectrum estimators can benefit from this scale separation. Moreover, the estimation of the power spectrum is computationally faster than the evaluation of its equivalent correlation function, which involves the aforementioned convolution and is only possible after the power spectrum is computed first. This gain in computational speed becomes an important factor when we sample a likelihood function numerous times in a high-dimensional parameter space.

Despite these advantages, most weak-lensing cosmological studies have been based on real-space correlation functions because the formal definition of the power spectrum involves integration angle from zero to infinity, which is not attainable in real observations. However, van Uitert et al. (2018) demonstrate that when they use band-limited power spectra, this weakness can be overcome. Below we summarize the formal definitions of the galaxy-mass and galaxy-galaxy power spectra and the corresponding band-limited power spectra used in the current analysis.

2.1. Galaxy-Mass Power Spectrum

The projected galaxy-mass power spectrum P^{gm} can be obtained from the matter power spectrum P_δ via the following relation:

$$P^{gm}(\ell) = b \left(\frac{3H_0^2 \Omega_m}{2c^2} \right) \int_0^{\chi_H} d\chi \times \frac{p_F(\chi)g(\chi)}{a(\chi)f_k(\chi)} P_\delta \left(\frac{\ell + 1/2}{f_k(\chi)}; \chi \right), \quad (1)$$

with b the effective linear galaxy bias⁹, H_0 the Hubble constant, Ω_m the present matter density, c the speed of light, χ the comoving distance, χ_H the comoving horizon distance, $a(\chi)$ the scale factor, f_k the comoving angular diameter distance, $p_F(\chi)$ the redshift distribution of foreground galaxies, and $g(\chi)$ a lensing efficiency (geometric weight) factor defined by

$$g(\chi) = \int_\chi^{\chi_H} d\chi' p_\chi(\chi') \frac{f_k(\chi' - \chi)}{f_k(\chi')}, \quad (2)$$

where $p_\chi(\chi)$ is the source redshift distribution $p_\chi(\chi)d\chi = p_z(z)dz$. This galaxy-mass power spectrum P^{gm} is also related to the mass-shear correlation (i.e., galaxy-galaxy lensing tangential shear) function $\gamma_T(\theta)$ via:

$$P^{gm}(\ell) = 2\pi \int_0^\infty d\theta \theta \gamma_T(\theta) J_2(\ell\theta), \quad (3)$$

where J_2 is the 2nd order Bessel function of the first kind.

Since the evaluation of Equation 3 requires our knowledge of γ_t over angles from zero to infinity, Equations 3 and 1 cannot be compared directly. Therefore, we use the following band power spectrum (as an estimator of $\ell^2 P^{gm}(\ell)$ for the i^{th} ℓ interval):

$$P_{band,i}^{gm} = \frac{1}{\Delta_i} \int_{\ell_{il}}^{\ell_{iu}} d\ell \ell P^{gm}(\ell) \quad (4)$$

$$= \frac{2\pi}{\Delta_i} \int_{\theta_{min}}^{\theta_{max}} \frac{d\theta}{\theta} \gamma_T(\theta) [h(\ell_{iu}\theta) - h(\ell_{il}\theta)] \quad (5)$$

with

$$h(x) = -xJ_1(x) - 2J_0(x), \quad (6)$$

where $J_{1(0)}$ is the first (zeroth) order Bessel function of the first kind, and

$$\Delta_i = \ln(\ell_{iu}/\ell_{il}), \quad (7)$$

where ℓ_{iu} and ℓ_{il} are the upper and lower limits of the i^{th} ℓ interval, respectively.

2.2. Intrinsic Alignment Contamination

The fundamental posit in weak-lensing is zero or negligible correlation of galaxy ellipticities in the absence of gravitational lensing. Certainly, this posit on intrinsic alignment (IA) becomes invalid in future surveys, where the interpretation is not limited by statistical errors. Cosmic shear studies from current precursor surveys have shown that although IA contamination causes

⁹ In general, galaxy bias depends on scale or mass. However, here b is the effective linear bias representing a collective value for the particular lens galaxy population.

a measurable shift in the best-fit parameter values, the amount of shift is still a small fraction of their statistical errors (e.g., Heymans et al. 2013; Hildebrandt et al. 2017; van Uitert et al. 2018). In galaxy-galaxy lensing, systematic errors due to the IA contamination can arise when lens-source pairs are physically close; large photometric redshift scatters make the lens-source separation imperfect. As these source galaxies tend to align radially toward the lens galaxies, in principle the IA contamination in galaxy-galaxy lensing leads to signal suppression. In the current study, we estimate the level of signal suppression using an IA model and find that the contamination is negligible and will not impact our cosmological parameter measurements. Below, we present the details.

As in Jee et al. (2016), we start with the following linear IA model of Catelan et al. (2001) and Hirata & Seljak (2004):

$$P_{\delta I}(z) = -A C_1 \rho_c \frac{\Omega_m}{D(z)} P_\delta(z), \quad (8)$$

where ρ_c is the critical density of the universe today, Ω_m is the matter density today, $P_\delta(z)$ is the linear matter power spectrum at z , A is a dimensionless IA amplitude, C_1 is the coefficient fixed to the value $C_1 = 5 \times 10^{-14} h^{-2} M_\odot^{-1} \text{Mpc}^3$, and $D(z)$ is the growth factor at z normalized to unity at $z = 0$. We replace the linear power spectrum P_δ in Equation 8 with a non-linear version, following Bridle & King (2007).

Once the nonlinear IA power spectrum $P_{\delta I}$ is obtained, the corresponding amplitude in the galaxy-mass power spectrum P^{gm} is estimated through Equation 1. For the fiducial amplitude $A = 1$, we find that the fractional change in P^{gm} is $\sim 0.5\%$, which is a factor of $30 \sim 50$ smaller than our statistical errors. Considering the typical range of marginalization of the IA amplitude ($A = -2 \sim 4$), we conclude that the IA contamination is clearly sub-dominant in our study. Note that the above IA power spectrum is slightly different from the one used in Jee et al. (2016), where we also considered the luminosity-dependence using the Joachimi et al. (2011) measurement. The added sophistication would be superfluous here because of the negligible IA contribution.

2.3. Galaxy Angular Power Spectrum

The galaxy angular power spectrum P^{gg} of the lens galaxies is evaluated from the matter power spectrum P_δ as below:

$$P^{gg}(\ell) = b^2 \int_0^{\chi_H} d\chi \frac{p_F^2(\chi)}{f_k^2(\chi)} P_\delta \left(\frac{\ell + 1/2}{f_k(\chi)}; \chi \right). \quad (9)$$

This galaxy angular power spectrum P^{gg} is related to the galaxy auto-correlation (often referred to as galaxy two-point correlation) function $w(\theta)$ through the following relation:

$$P^{gg}(\ell) = 2\pi \int_0^\infty d\theta \theta w(\theta) J_0(\ell\theta). \quad (10)$$

Analogously to the case of the galaxy-mass power spectrum P^{gm} , we define the band-limited power spectrum

for the galaxy angular power spectrum P^{gg} as follows:

$$P_{band,i}^{gg} = \frac{1}{\Delta_i} \int_{\ell_{ii}}^{\ell_{iu}} d\ell \ell P^{gg}(\ell) \quad (11)$$

$$= \frac{2\pi}{\Delta_i} \int_{\theta_{min}}^{\theta_{max}} \frac{d\theta}{\theta} w(\theta) [q(\ell_{iu}\theta) - q(\ell_{ii}\theta)] \quad (12)$$

with

$$q(x) = xJ_1(x). \quad (13)$$

Note that the equalities between Equations 4 and 5 and between Equations 11 and 12 are not always valid. The equalities depend on the choice of the θ_{min} and θ_{max} values for the given ℓ ranges. The valid ranges of θ_{min} and θ_{max} were investigated in Appendix A of van Uitert et al. (2018), who found that the estimate becomes slightly biased at the largest ℓ and applied corrections using theoretical predictions. In our power spectrum estimation, we also address these issues (§4.1).

3. DATA

3.1. Deep Lens Survey

The DLS is composed of five widely separated fields (F1-F5). The two fields (F1 and F2) in the northern hemisphere were observed with Mosaic-1 at the NOAO/KPNO 4m Mayall Telescope and the three fields (F3, F4, and F5) in the southern hemisphere were observed with Mosaic-2 at the NOAO/CTIO 4m Blanco Telescope. The locations of the field centers are summarized in Table 1. The total survey area is $\sim 20 \text{ deg}^2$ with each field covering $\sim 4 \text{ deg}^2$ ($\sim 2^\circ \times 2^\circ$). The DLS used more than ~ 120 nights on these 20 deg^2 areas in order to reach down to $\sim 26^{\text{th}}$ mag in BVz' bands and $\sim 27^{\text{th}}$ mag in R band (at the 5σ level), approaching the depth of LSST. The depth enables us to obtain high-fidelity photometric redshifts and galaxy shears. The R filter, where we measure galaxy shapes, was given priority whenever seeing is better than $\sim 0''.9$. The mean cumulative exposure time in R is $\sim 18,000$ s per field while in other filters the exposure time is $\sim 12,000$ s.

We utilized the photo- z data estimated with BPZ (Benítez et al. 2004) by Schmidt & Thorman (2013), who calibrated the priors and the spectral energy distribution (SED) templates using $\sim 10,000$ spectroscopic redshifts from the Smithsonian HEctospec Lensing Survey (SHELS; Geller et al. 2005) on F2. The fidelity of the photo- z estimations has been verified using an independent spectroscopic survey, PRIMUS Multi-object Survey (PRIMUS; Coil et al. 2011) on F5 by Schmidt & Thorman (2013) and Jee et al. (2013). The DLS galaxy shape catalog was obtained by fitting a PSF-convolved elliptical Gaussian to each galaxy image. The PSF was modelled by principal component analysis (PCA) method (Jee & Tyson 2011). We refer readers to Jee et al. (2013) for shape measurement details.

3.2. Lens and Source Selection

For measuring galaxy-galaxy lensing signals, we define two lens bins (L1, L2) and two source bins (S1, S2) over broad redshift ranges. To select galaxies in each bin, we use the peak redshift value (z_b) whereas for calculating the theoretical power spectrum, we stack the photometric

Table 1
DLS Field Centers (J2000)

Field	RA	Dec	l, b
F1	00 ^h 53 ^m 25.3 ^s	+12°33'55"	125°, -50°
F2	09 ^h 19 ^m 32.4 ^s	+30°00'00"	197°, 44°
F3	05 ^h 20 ^m 00 ^s	-49°00'00"	255°, -35°
F4	10 ^h 52 ^m 00 ^s	-05°00'00"	257°, 47°
F5	13 ^h 59 ^m 20 ^s	-11°03'00"	328°, 49°

redshift probability distribution $p(z)$ of individual galaxies (output by BPZ) to estimate the redshift distribution for each bin; a noticeable reduction of photo- z bias when one uses $p(z)$ instead single-point estimates is shown in Wittman (2009) and Schmidt & Thorman (2013).

The redshift range of our lens galaxies is $0.15 < z_b < 0.75$; we avoid galaxies whose z_b is less than 0.15 because of a large discrepancy between photometric and spectroscopic redshifts in that low-redshift range (Jee et al. 2013). This lens redshift interval is divided into two lens bins: L1 ($0.15 < z_b < 0.4$) and L2 ($0.4 < z_b < 0.75$). Although our using the stacked $p(z)$ curve instead of a collection of the z_b values reduces the photo- z bias, our detailed comparisons with the spectroscopic catalogs reveal that the mean redshift of the lens population in L1 would still be biased low by $\sim 10\%$ if left uncorrected whereas the bias would be negligible ($\sim 1\%$) in L2 (see Appendix A). Therefore, in our cosmological parameter estimation we apply this $p(z)$ calibration to the L1 population in such a way that the means agree. We find that if this $p(z)$ calibration were omitted, our estimation of S_8 would be biased high by ~ 0.02 , which corresponds to $\sim 50\%$ of the statistical error.

We adopt the magnitude lower limit $m_R = 18$ of Choi et al. (2012) for both lens bins while we use the upper limits $m_R=21$ and 22 for L1 and L2, respectively. Unlike Choi et al. (2012), we, however, do not use absolute magnitudes as selection criteria because large photometric redshift scatters of individual galaxies can cause noise amplification. Stars are removed using the size-magnitude relation and shape criteria as described in Jee et al. (2013).

We define source galaxies as follows. The redshift range is chosen to be $0.4 < z_b < 1.5$. The choice of the photo- z upper limit is motivated by the DLS filters (BVRz') and the maximum redshift ($z \sim 1.2$) of our photometric-spectroscopic redshift comparison sample. The interval is divided into two source bins: S1 ($0.4 < z_b < 0.75$) and S2 ($0.75 < z_b < 1.5$). The redshift range of the first source bin overlaps with that of the second lens bin. Therefore, we do not use the L2-S1 combination to measure lensing signals. The upper limit of the source magnitude is $m_R = 24.5$, which corresponds to the approximate upper limit of the photometric-spectroscopic redshift comparison (Schmidt & Thorman 2013). According to the weak-lensing image simulation of Jee et al. (2013), galaxies at $m_R > 24.5$ require a large multiplicative factor in shear calibration. Therefore, applying this magnitude cut is our conservative measure to minimize the impact of our shear calibration and photo- z uncertainties; we note that Jee et al. (2013, 2016) used source galaxies up to $m_R \sim 26$. Because we measure shears from source

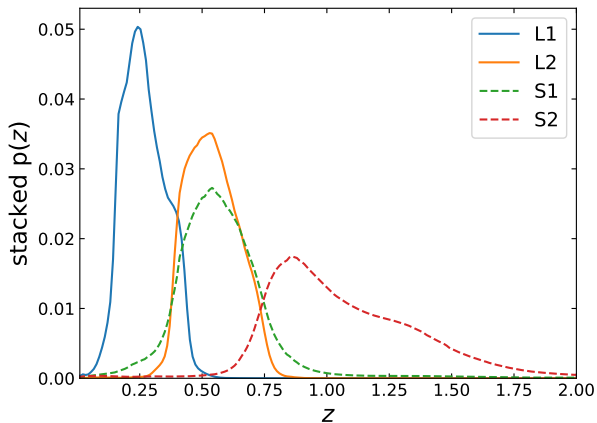


Figure 2. Redshift distributions of lens and source galaxies. The distribution in each bin is estimated by stacking the $p(z)$ curves of individual galaxies. We normalize the curves in such a way that their integrated areas are identical.

Table 2
Lens & Source Selection

	bins	z_b^-	z_b^+	$\langle z \rangle$	m_R^-	m_R^+	# of gal
Lens	L1	0.15	0.4	0.270	18	21	57,802
	L2	0.4	0.75	0.542	18	22	98,267
Source	S1	0.4	0.75	0.642	21	24.5	418,932
	S2	0.75	1.5	1.088	21	24.5	450,353

galaxies, we also need to apply shape criteria. As in Jee et al. (2013, 2016), we require the semi-minor axis of the best-fit (PSF-corrected) elliptical Gaussian to be larger than 0.4 pixels. In addition, we select sources whose ellipticity measurement error ($\sigma_{e,i}$) is less than 0.3.

Table 2 summarizes our selection criteria and the resulting number of galaxies in each bin. The stacked redshift distribution of each bin is presented in Figure 2.

3.3. Shear Calibration and Tangential Shear Measurement

In general, weak-lensing shears are derived by measuring galaxy ellipticities and taking averages over populations. A number of issues cause the average ellipticity to deviate from the true shear. Well-known difficulties include inaccurate point spread function (PSF) modeling, nonlinear relation between pixel noise and ellipticity (noise bias), discrepancy between galaxy model and real profiles (model bias), selection bias, incomplete deblending, etc. Since the application of weak lensing to cosmology requires a sub-percent level accuracy in shear measurement, the community has invested significant efforts to develop and test various shear measurement techniques. The most prominent efforts include the public blind shear measurement challenge programs, in which weak-lensing practitioners participate in analyzing and measuring weak-lensing shears from computer-generated galaxy images; the participants are blind to input shears. A variant of the DLS weak-lensing pipeline participated in the most recent public shear measurement challenge called the third GRavitational lEnsing Accuracy Testing (GREAT3; Mandelbaum et al. 2015) and won the chal-

lenge. The details of the galaxy shape measurement and shear calibration procedures are described in Jee et al. (2013). Here we present the summary.

The DLS galaxy shapes are measured by fitting elliptical Gaussian profiles. The ellipticity g is determined with the semi-major α and semi-minor β axes using the relation $g = (\alpha - \beta)/(\alpha + \beta)$. The PSF effect is addressed by convolving the elliptical Gaussian with the model PSF prior to fitting. As mentioned above, the discrepancy between the Gaussian model and real galaxy profiles (model bias) is a non-negligible source of bias in shear estimation. Also, because of nonlinear coupling between pixel noise and shape parameter uncertainties, noise bias arises. Jee et al. (2013) address these shear calibration issues through image simulations (Jee & Tyson 2011) using real galaxy images from the Hubble Ultra Deep Field (HUDF; Beckwith et al. 2006). They determine the two shear calibration parameters in the following equation:

$$\gamma^{true} = m_\gamma \gamma^{obs} + C, \quad (14)$$

where γ^{true} and γ^{obs} are true and observed shears, respectively, m_γ is a multiplicative correction parameter¹⁰, and C is an additive correction parameter. As the DLS additive correction is negligibly small ($\sim 10^{-4}$), we only apply the multiplicative correction (Jee et al. 2013). In principle, shear calibration is a function of many parameters such as PSF size, galaxy size and morphology, magnitude, noise level, etc. However, characterizing shear calibration with a large number of parameters is not feasible because of the limited number of galaxies in the HUDF; the result would be dominated by random fluctuations rather than by real trends. Therefore, we use the following single-parameter characterization:

$$m_\gamma = 6 \times 10^{-4} (m_R - 20)^{3.26} + 1.036, \quad (15)$$

where m_R is the source magnitude. This procedure is a good approximation because we conserve the HUDF galaxy properties such as size, morphology, etc. as a function of magnitude in our image simulations.

After the application of the above shear calibration, we derive tangential shears as follows. For each lens-source pair, a tangential shear is defined through:

$$g_T = -g_1 \cos 2\phi - g_2 \sin 2\phi \quad (16)$$

where g_1 and g_2 are the two components of the source galaxy ellipticity and ϕ is the position angle (measured counterclockwise) of the vector from the lens to the source with respect to a reference axis.

Obviously, a signal from a single lens-source pair is too small to detect, and thus it is necessary to stack signals over all lens-source pairs as follows:

$$\gamma_T^{raw}(\theta) = \frac{\sum_{i,j} g_{T,ij} w_i}{\sum_{i,j} w_i}, \quad (17)$$

where $g_{T,ij}$ is the tangential shear of the i^{th} source galaxy with respect to the j^{th} lens galaxy, θ is the distance between the lens-source pair, and w_i is the inverse variance

¹⁰ Some authors prefer to use $m'_\gamma = m_\gamma - 1$ as the definition of the shear multiplicative bias.

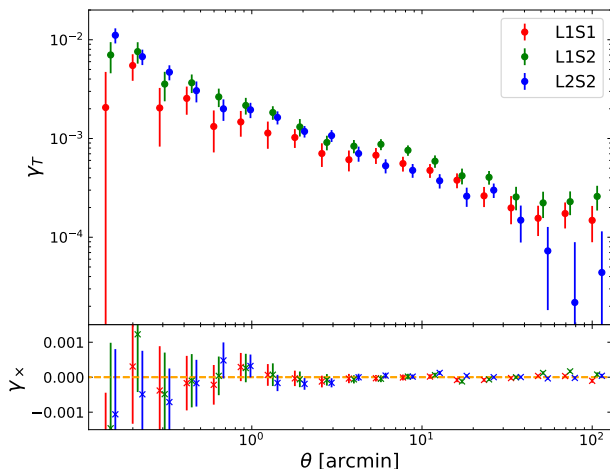


Figure 3. DLS shear measurement. Top: tangential shear profiles measured for the lens-source pairs, L1-S1, L1-S2 and L2-S2. Bottom: cross (45°-rotated) shears measured to check residual systematics. The consistency of cross shears with zero shows that the shear additive errors are nicely controlled. The error bars estimated with our log-normal field simulations include the impact of shot noise (shape noise), field masks/boundaries, and the sample variance.

weight:

$$w_i = \frac{1}{\sigma_{e,i}^2 + \sigma_{SN}^2}. \quad (18)$$

In Equation 18, $\sigma_{e,i}$ is the ellipticity measurement error for the i^{th} source galaxy and σ_{SN} is the ellipticity dispersion (shape noise) of the source population.

Galaxy density fluctuations due to various masks and field boundaries increase the sample variance and also hamper the cancelling effects of residual additive biases in shear calibration through azimuthal averaging. To address the issue, we adopt the suggestion of Singh et al. (2017) and subtract random catalog signals from the above raw tangential shears as follows:

$$\langle \gamma_T(\theta) \rangle = \langle \gamma_T^{\text{raw}}(\theta) \rangle - \langle \gamma_T^{\text{random}}(\theta) \rangle. \quad (19)$$

We find that this correction is important for tangential shear measurements on large scales ($\theta \gtrsim 30'$) as shown in Appendix B. We use the **Athena** code¹¹ for measuring tangential shears and the **venice** code¹² to generate the random points while taking care of star masks and field boundaries.

We present our tangential shears for the L1-S1, L1-S2, and L2-S2 pairs in Figure 3. As mentioned above, the displayed tangential shears are obtained after application of the random signal subtraction (Equation 19). The error bars are estimated with the log-normal field simulations (§4.2) and include the impact of shot noise (shape noise), field masks/boundaries, and the sample variance.

To test residual lensing systematics, it is useful to examine cross shears, which are obtained by rotating source galaxy images by 45 degrees (the bottom panel of Figure 3). As shown, they are consistent with zero on all

¹¹ <http://www.cosmostat.org/software/athena>

¹² <https://github.com/jcoupon/venice>

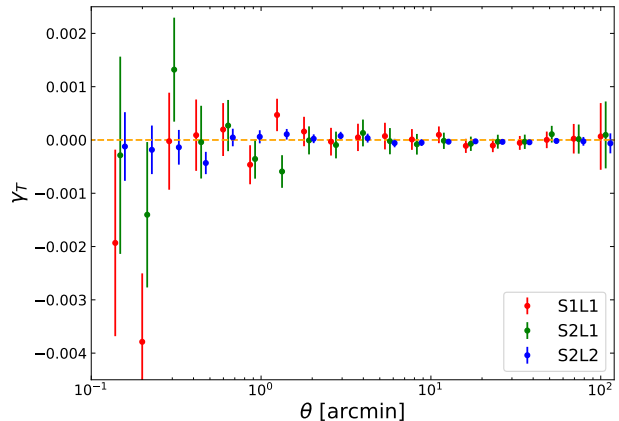


Figure 4. Lens-source flip test. The displayed signals are constructed by measuring tangential shears around source galaxies with lens galaxy shapes. Without the presence of measurable systematic errors in shear and photo- z estimation, the resulting signals should vanish as shown. The errors are estimated with a 20×20 block jackknifing in each field.

scales for every lens-source bin pair, supporting the reliability of our tangential shear measurements.

Another way to check residual systematics is the lens-source flip test, which examines the fidelity of both photo- z estimation and shear measurement. In this test, lens and source bins are switched. That is, we measure tangential shears around source galaxies using lens galaxy shapes. If their redshift distributions indeed do not overlap significantly, as shown in Figure 2, the resulting signals should vanish. However, residual systematic errors in photometric redshift and/or shear measurements would produce signals with non-zero amplitude. We perform this test for all three lens-source bin pairs, and the results are consistent with zero (Figure 4).

3.4. Galaxy Angular Correlation Measurement

The angular correlation function $w(\theta)$ is an excess probability of finding galaxies at a distance of θ with respect to that in a Poisson distribution:

$$dP = N[1 + w(\theta)]d\Omega, \quad (20)$$

where N is the mean number density of galaxies and dP is the total expected number of galaxies at a distance θ within the solid angle $d\Omega$. If a galaxy bias is known, $w(\theta)$ alone can constrain cosmological parameters. In the current study, this galaxy bias is constrained by combining the galaxy clustering information with the galaxy-galaxy lensing signal.

In order to reduce systematic errors in the estimation of $w(\theta)$, a number of estimators have been suggested. We use the following estimator of Landy & Szalay (1993):

$$w(\theta) = \frac{\langle DD \rangle + \langle RR \rangle - 2\langle DR \rangle}{\langle RR \rangle}, \quad (21)$$

where $\langle DD \rangle$, $\langle DR \rangle$, and $\langle RR \rangle$ are the number of galaxy-galaxy pairs, galaxy-random pairs, and random-random pairs, respectively.

When we blindly apply the above estimator to observational data with small areas, the amplitude of $w(\theta)$ is slightly underestimated by an additive factor known as

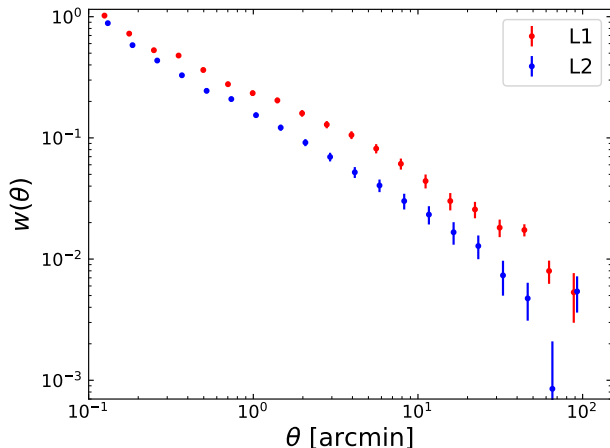


Figure 5. Galaxy angular correlation measured in the two lens bins L1 and L2. We use the Landy & Szalay (1993) estimator. The error bars are estimated using our log-normal field simulations, which include shot noise, field masking/boundaries, and the sample variance. IC corrections are included using Equation 22.

the “integral constraint”. The deficit occurs because the average number of galaxies in the finite-size field becomes the reference to measure the excess probability. To correct for this bias, one should add the following constant (Roche & Eales 1999):

$$IC = \frac{1}{\Omega^2} \int w_{true}(\theta) d\Omega_1 d\Omega_2, \quad (22)$$

where $d\Omega_1$ and $d\Omega_2$ are two small patches within the observational field with the angular separation θ , w_{true} is the true angular correlation function, and the integral is evaluated over the entire observational field. Although in the current study we assume the Planck2015 cosmology to calculate $w_{true}(\theta)$, we verify that the cosmology-dependence of the correction is negligibly small (§5.2). The estimated IC values for L1 and L2 are 0.0126 and 0.0062, respectively.

The galaxy angular correlations for the two lens bins L1 and L2 are plotted in Figure 5. As is done with the galaxy-shear correlations (§3.4), the error bars are estimated using our log-normal field simulations, which include various observational effects such as galaxy shot noise and field masks/boundaries, as well as the sample variance. The galaxy angular correlations are measured in 20 logarithmic bins from $0.1'$ to $100'$. The displayed correlation functions include the aforementioned integral constraints (Equation 22).

4. RESULTS

4.1. Power Spectrum Reconstruction

Following Equations 5 and 12, we transform the tangential shear measurement $\gamma_T(\theta)$ to the band galaxy-mass power spectrum $P_{band}^{gm}(\ell)$ and the angular correlation function $w(\theta)$ to the band galaxy angular power spectrum $P_{band}^{gg}(\ell)$, respectively.

The range of the integral for P_{band}^{gm} (Equation 5) is from $0.14'$ to $100'$ and the one for P_{band}^{gg} (Equation 12) is from $0.12'$ to $84'$. The centers of the logarithmic ℓ bins are $\ell = 251, 399, 632, 1002, \text{ and } 1589$ for P_{band}^{gg} and $\ell = 314, 498, 790, 1252, \text{ and } 1985$ for P_{band}^{gm} . The different θ ranges and

the corresponding ℓ ranges for P_{band}^{gg} and P_{band}^{gm} are deliberate choices. As briefly mentioned in §2.3, in order to accurately reconstruct a band power spectrum for each ℓ bin, van Uitert et al. (2018) investigated valid θ ranges (see Appendix A of their paper). We repeat the experiment of van Uitert et al. (2018) using our DLS photometric redshifts and θ ranges and find that for the highest ℓ bin P_{band}^{gm} allows θ_{min} as large as $\sim 2'$, whereas P_{band}^{gg} requires $\theta_{min} \lesssim 0.2'$. On the other hand, the power spectrum evaluation at lowest ℓ bins requires the knowledge of $w(\theta)$ and $\gamma_T(\theta)$ at large angles. In order to address the issue, we attach “tails” of theoretically estimated $w(\theta)$ and $\gamma_T(\theta)$ for the ranges from $85'$ to $424'$ and from $100'$ to $493'$, respectively. Here we use the Planck2015 cosmology for the computation. Although the exact values of the attached tails depend on cosmology, we verify that the impact of the assumed cosmology on our cosmological parameter determination is insignificant (§5.2).

The reconstructed power spectra are presented in Figure 6 with $1-\sigma$ error bars. The solid lines (Equations 1 and 9) show theoretical (including baryonic feedback effect and neutrino masses, §4.3.2) band power spectra computed at continuous ℓ ranges with the best-fit parameters (§4.3.4). The shaded regions represent the variations of the theoretical lines when the $1-\sigma$ uncertainties of the two galaxy bias parameters b_1 and b_2 are considered. In galaxy angular power spectrum, this uncertainty is magnified because the galaxy angular power spectrum is proportional to the galaxy bias squared ($P_{band}^{gg} \propto b^2 P_{\delta}$) whereas the galaxy-mass power spectrum is linear with the galaxy bias ($P_{band}^{gm} \propto b P_{\delta}$).

For our likelihood evaluation (§4.3.1), we define a power spectrum data vector \mathbf{p}_d with the reconstructed band power spectra using the following ordering:

$$\mathbf{p}_d = [P_{L1}^{gg}, P_{L2}^{gg}, P_{L1S1}^{gm}, P_{L1S2}^{gm}, P_{L2S2}^{gm}]. \quad (23)$$

Since each band power spectrum is measured at five ℓ bins, the \mathbf{p}_d vector is composed of 25 elements.

4.2. Covariance Estimation

In cosmological parameter estimation with a weak lensing survey, robust construction of a covariance matrix is paramount. The covariance should include the effects of galaxy shape noise, field maskings, boundary shapes, weak-lensing systematics, sample variances, etc. There have been a number of suggestions for the estimation of the covariance matrix. In the linear regime, it is possible to derive the survey covariance analytically using Gaussian assumptions. The use of numerical simulations and ray-tracing methods has been a popular choice because the resulting covariance is valid in the nonlinear regime and one can easily incorporate observational features such as survey geometry, masking, etc. Another powerful method for producing high-fidelity covariances is to simulate weak-lensing galaxy catalogs using log-normal approximations, which is our choice in the current study.

Approximation of the large scale structure of the universe with a log-normal distribution has been a popular choice (e.g., Hubble 1934; Peebles 1980; Coles & Jones 1991; Gaztanaga & Yokoyama 1993; Taylor & Watts 2000; Kayo et al. 2001; Jasche et al. 2010; Hilbert et al. 2011; Alonso et al. 2014). In this study, we use the Full-

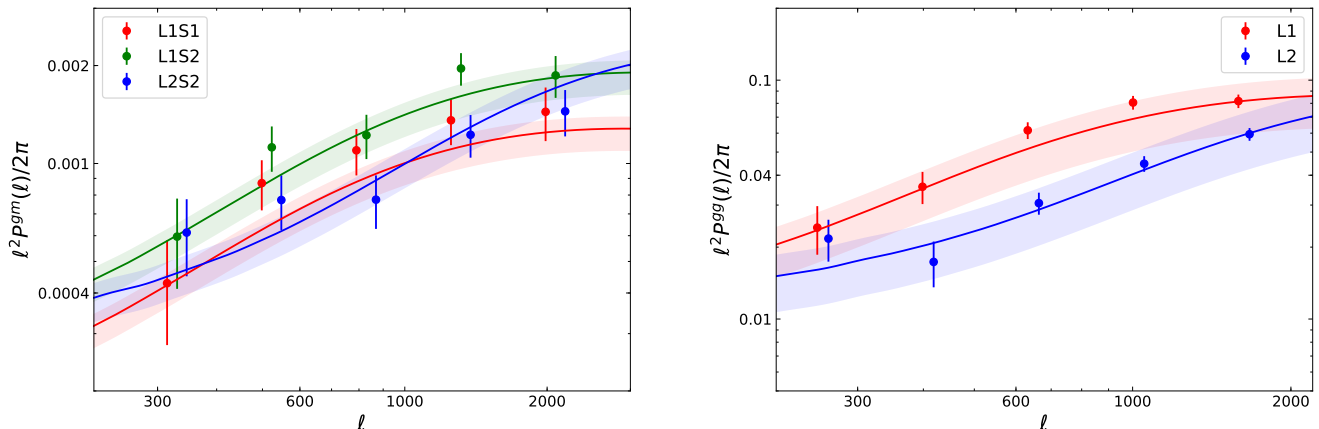


Figure 6. Observed DLS band power spectrum. left: galaxy-mass power spectrum P^{gm} for the three lens-source pairs, L1-S1, L1-S2, and L2-S2. right: galaxy angular power spectrum for the two lens bins, L1 and L2. The ℓ bins are centered at $\ell = 251, 399, 632, 1002,$ and 1589 for P^{gg} and $\ell = 314, 498, 790, 1252,$ and 1985 for P^{gm} . Slight horizontal shifts are applied to avoid clutter. Solid lines show theoretical predictions with the best-fit cosmological parameters. The error bars are $1\text{-}\sigma$ ranges estimated using our log-normal field simulations. The offsets between the measurements and the best-fit lines are not statistically significant when we take into account of large uncertainty of galaxy biases b whose $1\text{-}\sigma$ levels are shown as shaded regions around the solid lines.

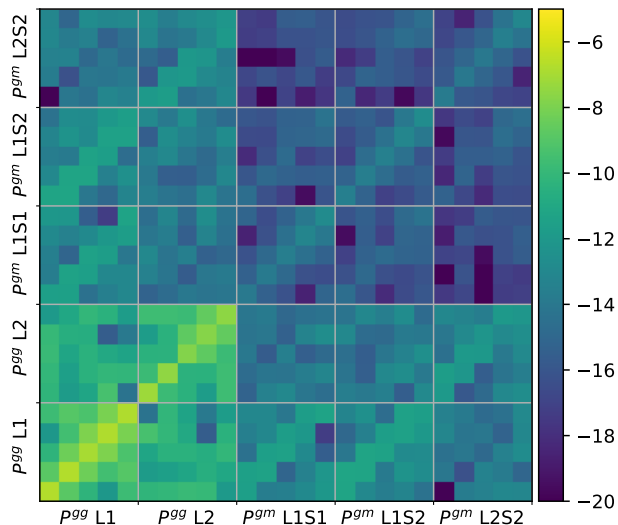


Figure 7. Covariance of the DLS band power spectrum. The covariance is estimated based on 100 FLASK simulations for each field (F1-F5). The ordering of the covariances are the galaxy angular power spectra P^{gg} from L1 and L2 and the galaxy-mass power spectra P^{gm} from the L1-S1, L1-S2, and L2-S2 pairs. Since each power spectrum has five ℓ bins, the total dimension of the covariance matrix is 25 by 25. The dominance of the (sub-)diagonal elements indicates that different scales are well separated; note that the level is depicted in a log scale.

sky Lognormal Astro-fields Simulation Kit¹³ (FLASK; Xavier et al. 2016). FLASK is useful for conveniently generating galaxy catalogs with a large sky coverage while including observational features. We use FLASK to estimate covariances for our galaxy-galaxy and galaxy-mass power spectra.

FLASK generates catalogs that contain galaxy posi-

tions and shapes based on log-normal distributions, taking all combinations of galaxy-galaxy, galaxy-mass, and matter power spectrum between all lens and source bins as inputs. We produce 100 mock fields for each DLS field. To mimic the DLS observational features, we provide FLASK with the stacked photo- z distributions for lenses and source bins, source density, galaxy shape dispersion, star masks, and field boundaries.

The resulting FLASK catalogs are processed with the same analysis pipeline that is used for the DLS correlation function measurements in the current study and are converted to band power spectra. These power spectra from different realizations are combined to produce power spectrum covariances. The covariance matrix obtained in this way is shown in Figure 7. The ordering of the covariances are the galaxy-galaxy power spectra P^{gg} from L1 and L2 and the galaxy-mass power spectra P^{gm} from the L1-S1, L1-S2, and L2-S2 pairs. Since each power spectrum has five ℓ bins, the total dimension of the covariance matrix is 25×25 . The dominance of the diagonal elements shows that the signals on different scales are only weakly correlated.

The covariance matrix \mathbf{C} obtained above can be utilized to quantify the *raw* signal-to-noise ratio (S/N), which is defined as:

$$\frac{S}{N} = (\mathbf{p}_d^T \mathbf{C}^{-1} \mathbf{p}_d)^{1/2}, \quad (24)$$

where \mathbf{p}_d is the data vector containing our observed band power spectra (§4.1). According to Equation 24, the *raw* total S/N of our band power spectra from the DLS is 30.6. At face value this S/N estimate is higher than the one ($S/N = 21.5$) for the DLS cosmic shear data presented in Jee et al. (2016). However, we note that this larger S/N value does not directly translate to smaller parameter uncertainties because the two studies use different nuisance parameters (e.g., two galaxy bias parameters) and suffer from different degeneracies.

4.3. Cosmological Parameter Constraints

¹³ <http://www.astro.iag.usp.br/~flask>

4.3.1. Likelihood Sampling

Our cosmological parameters are estimated by sampling the following likelihood function:

$$\mathcal{L} = \frac{1}{(2\pi)^{n/2} |\mathbf{C}|^{1/2}} \exp \left[-\frac{1}{2} (\mathbf{p}_d - \mathbf{p}_{th})^T \mathbf{C}^{-1} (\mathbf{p}_d - \mathbf{p}_{th}) \right], \quad (25)$$

where \mathbf{p}_{th} is the theory vector predicted for a given set of cosmological parameters, n is the number of elements in the vector, and \mathbf{C} is the covariance matrix discussed in §4.2. Although the covariance depends on cosmology, it is treated as a constant in our parameter estimation (thus we ignore the determinant $|\mathbf{C}|$). We quantify the cosmology dependence in §5.

One practical issue in deriving parameter constraints from the above likelihood is the sampling efficiency when the dimension is large and the likelihood function evaluation is computationally expensive. The traditional de facto standard tool is the Markov Chain Monte Carlo (MCMC) algorithm, which samples the likelihood in a high-dimensional parameter space based on a random walk. Thanks to increasing availability in parallelization, these time-consuming computations can be achieved within a reasonable amount of time. However, when one’s interest is not only the inference (parameter value estimation), but also the model selection using Bayesian approach, one needs to compute Bayes factors, which require at least an order-of-magnitude more likelihood evaluations.

To overcome this computational challenge in Bayesian evidence estimation, one needs more efficient sampling algorithms than the traditional MCMC. In our study, we employ the nested sampling algorithm (Skilling 2006), which outputs Bayesian evidence with much greater efficiency and provides parameter constraints as its byproducts. More specifically, we use the `multinest`¹⁴ package (Feroz et al. 2009), which has been widely applied and tested in many cosmological studies such as Troxel et al. (2017), Köhlinger et al. (2017), Chisari et al. (2018), etc.

4.3.2. Power Spectrum and Baryonic Effects

Robust evaluation of the theory vector \mathbf{p}_{th} in Equation 25 requires the accurate knowledge of the nonlinear matter power spectrum (Equations 1 and 9). In our previous cosmic shear studies (Jee et al. 2013, 2016), we use the Eisenstein & Hu (1998) transfer function and the Smith et al. (2003) “halofit” nonlinear power spectrum correction. Experimenting with the Takahashi et al. (2012) version, which improved the accuracy of the Smith et al. (2003) power spectrum based on higher resolution N-body simulations, Jee et al. (2016) find that the $S_8 = \sigma_8(\Omega_m/0.3)^{0.5}$ value decreases by ~ 0.02 , consistent with the findings of MacCrann et al. (2015), who performed the comparison using the CFHTLenS lensing catalog. The weakness of these “halofit” approaches was that the result is valid only within a narrow range of cosmological parameters. Mead et al. (2015) improve the applicability of the “halofit” formalism by fitting physically-motivated free parameters to a wide range of cosmological high-resolution N-body simulations. The extra degrees of freedom allow Mead et al. (2015) to apply the method even to simulations with various baryonic effects. They show that it is possible for the model to accommodate varying degrees of baryonic effects with a single parameter using the relation between the two free parameters η_0 and A_{baryon} :

$$\eta_0 = 0.98 - 0.12 A_{baryon}, \quad (26)$$

where η_0 is a parameter characterizing η , which is referred to as the halo “bloating” parameter in Mead et al. (2015).

¹⁴ <https://github.com/JohannesBuchner/MultiNest>

Table 3
Prior Ranges Used in Cosmological Parameter Estimation

parameters	prior range	
Nuisance parameters		
photo- z shift in L1, L2, S1, S2 (σ_{zi}), $\mathcal{N}(0,0.02)$	-0.04	0.04
multiplicative shear error (m_γ)	-0.03	0.03
Astrophysical parameters		
galaxy bias in L1 & L2 (b_i)	0.1	2.5
baryon amplitude (A_{baryon})	2.0	4.0
Cosmological parameters		
matter density (Ω_m)	0.1	1.0
baryon density (Ω_b)	0.03	0.06
hubble parameter (h)	0.55	0.85
power spectrum normalization (σ_8)	0.1	1.5
spectral index (n_s)	0.9	1.04
sum of neutrino masses ($\Sigma_\nu m_\nu/\text{eV}$)	0.06	0.9

Note. — Displayed are the prior ranges of the 14 parameters used in our cosmological parameter estimation for the flat Λ CDM model (five nuisance, three astrophysical, and six cosmological parameters). Only photo- z shifts employ Gaussian priors while others use flat priors.

The parameter A_{baryon} characterizes the relation between the concentration $C(M, z)$ of a halo with a mass M at a redshift z and its formation redshift z_f via $C(M, z) = A_{baryon}(1+z_f)/(1+z)$. The best fit values of A_{baryon} are 3.13 for dark matter only simulation and 2.32 for the case with AGN feedback included. Note that Equation 26 shows the updated result (A. Mead, in private communication) and is slightly different from the original relation published in Mead et al. (2015). This flexibility of the Mead et al. (2015) approach provides an opportunity to investigate the impact of the baryonic physics on our power spectrum. In our cosmological parameter estimation, we use the Mead et al. (2015) nonlinear power spectrum while marginalizing over the interval $2 < A_{baryon} < 4$, which brackets the AGN feedback result from the OverWhelmingly Large cosmological hydrodynamical Simulations (OWLS; Schaye et al. 2010; van Daalen et al. 2011) and dark matter-only results. To implement this, we modified the `camb` and `pycamb` packages so that we can pass the A_{baryon} parameter from `pycamb` to `HMcode`¹⁵, which computes the Mead et al. (2015) power spectrum.

According to the current state-of-the-art cosmological hydro-simulations (e.g., van Daalen et al. 2011; Vogelsberger et al. 2014; Dubois et al. 2014; Springel et al. 2018), AGN feedback suppresses the amplitude of the matter power spectrum substantially at $k > 1 h \text{ Mpc}^{-1}$ (e.g., Chisari et al. 2018). When we examine the fractional change in P^{gg} and P^{gm} resulting from this matter power spectrum suppression corresponding to the OWLS simulation, we find that the effect is significant (5–20%) across our entire ($250 \lesssim \ell \lesssim 2000$) multipole range. We present the quantitative comparison in Appendix C.

4.3.3. Prior Ranges

We define five nuisance parameters to address systematic uncertainties. To account for photo- z systematic errors, we parameterize the photometric redshift probability of the lens and source redshift bins in the following way:

$$p_i(z) = p_i^o [(1 + \sigma_{zi})z], \quad (27)$$

¹⁵ <https://github.com/alexander-mead/HMcode>

where $p_i^o(z)$ is the observed (fixed) photometric redshift probability for the i^{th} bin (derived from stacking the BPZ $p(z)$ curves of individual galaxies) and $p_i(z)$ is the randomized photometric redshift probability after the $z \rightarrow (1 + \sigma_{zi})z$ mapping. We let σ_{zi} vary within the interval $[-0.04, 0.04]$ following a zero-centered Gaussian distribution with a standard deviation of 0.02. This is based on the DLS photo- z bias estimated by Schmidt & Thorman (2013). Similar effects on parameter constraints are found when we instead applied $\pm 3\%$ flat prior employed in Jee et al. (2013, 2016); this 3% flat prior was motivated by the 3% difference measured in photometric redshift comparison between the VIMOS-VLT Deep Survey and the Hubble Deep Field North (HDF-N) priors. Since we have two redshifts bins for both lens and source, the total number of the σ_{zi} parameters is four. When marginalizing over the multiplicative shear calibration bias m_γ , we assume a 3% flat prior as in our cosmic shear studies (Jee et al. 2013, 2016).

For the two galaxy bias parameters b_1 and b_2 , we apply a flat prior ranging from 0.1 to 2.5. These two parameters are highly degenerate with Ω_m and σ_8 and thus require sufficiently large intervals to minimize parameter estimation bias imposed by the prior interval. We verify that both bias parameters are constrained well within this prior interval and enlarging it further does not change our results.

Our main cosmological parameter constraints are obtained for a flat Λ CDM universe with baryonic feedback. For Ω_m and σ_8 , we use the prior intervals $[0.1, 1.0]$ and $[0.1, 1.5]$, respectively. Similarly to b_1 and b_2 , these two cosmological parameters are well constrained within the prior ranges. For the Hubble constant, we use the interval $[0.55, 0.85]$, which brackets the 4- σ lower- and upper-limits of both the Planck and direct measurements (Planck Collaboration et al. 2016; Riess et al. 2018). Our prior for the scalar spectral index n_s varies with a uniform probability within $[0.9, 1.04]$, again well encompassing the current constraints.

Currently, the most uncertain model parameter is A_{baryon} . According to Mead et al. (2015) who base their analysis on the OWLS results, the power spectrum from the dark matter-only simulation corresponds to $A_{\text{baryon}} = 3.13^{16}$. For a simulation that has prescriptions for baryonic physics such as gas cooling, heating, star formation and evolution, chemical enrichment, and supernovae feedback (however without AGN feedback), the preferred value slightly increases to $A_{\text{baryon}} = 3.91$, which nevertheless is not a statistically meaningful difference from the former case. A significant change occurs when the prescription includes AGN feedback, which reduces A_{baryon} to 2.32. Since currently there is no consensus on the exact impact of baryonic feedback (e.g., Chisari et al. 2018), we rely on the Mead et al. (2015) results based on the OWLS simulations and choose A_{baryon} to vary within the interval $[2, 4]$, which brackets both the dark matter only simulation case ($A_{\text{baryon}} = 3.13$) and the largest departure from it ($A_{\text{baryon}} = 2.32$). Note that the same interval $[2, 4]$ is also used in Hildebrandt et al. (2017) and Joudaki et al. (2017a).

Finally, we marginalize over a sum of neutrino masses ($\Sigma_\nu \mu_\nu$) within the flat prior range $[0.06 \text{ eV}, 0.9 \text{ eV}]$. The theoretical lower limit is $\sim 0.06 \text{ eV}$ for standard-model active neutrinos with the normal hierarchy. According to Planck2015, the upper limit of the 95% confidence regions for the sum of neutrino masses varies from $\sim 0.2 \text{ eV}$ to $\sim 0.7 \text{ eV}$ depending on the combinations of the Planck power spectra, Planck lensing, and external data. Thus, our prior range $[0.06 \text{ eV}, 0.9 \text{ eV}]$ amply brackets the current theoretical and observa-

tional constraints. Including neutrino masses are important because similarly to baryonic feedback, massive neutrinos also suppress the amplitude of the power spectrum on small scales (Appendix D). For simplification, we consider the case with one massive neutrino and two zero-mass neutrino species.

For our baseline cosmology (flat Λ CDM), the total number of parameters is 14 (five nuisance, three astrophysical, and six cosmological parameters). We summarize their prior ranges in Table 3.

4.3.4. Parameter Estimation Results

Figure 8 displays our parameter constraint results. The constrained parameters are the matter density (Ω_m), normalization (σ_8), and two effective galaxy bias parameters b_1 and b_2 ; the $S_8 \equiv \sigma_8(\Omega_m/0.3)^{0.5}$ parameter is not independent. It is clear that those four constrained parameters are highly degenerate with one another. The degeneracy between Ω_m and σ_8 arises because the overall power spectrum amplitude A_p measured by weak lensing is $A_p \sim \sigma_8 \Omega_m^\alpha$, where the exponent α is ~ 0.5 . This motivates the definition of $S_8 \equiv \sigma_8(\Omega_m/0.3)^{0.5}$, which is useful when results from different studies are compared. The current DLS G³M constraint with baryonic feedback marginalization is $S_8 = 0.818^{+0.031}_{-0.039}$ while without the marginalization we obtain a lower value $S_8 = 0.763^{+0.030}_{-0.040}$. The shift in S_8 arises from the power spectrum suppression due to the baryonic feedback (Appendix C).

The DLS G³M constraint is in good agreement with the value derived from the DLS tomographic cosmic shear $S_8 = 0.818^{+0.034}_{-0.026}$ (Jee et al. 2016) as shown in Figure 9. Since the DLS cosmic shear result was obtained without marginalizing over the baryonic effect parameter, we expect that the S_8 value would increase slightly when we repeat the analysis with the same marginalization, which is the subject of a future investigation. The S_8 uncertainty from the cosmic shear is $\sim 86\%$ of the G³M uncertainty. However, this S_8 uncertainty alone should not be used to judge the overall S/N of the DLS G³M data because S_8 is a measure of the parameter constraints in a particular projection and its uncertainty is proportional to the width of the Ω_m - σ_8 “banana”. One way to compare the Ω_m - σ_8 degeneracy breaking power (i.e., reducing the length of the “banana”) is simply to compare the uncertainties of the marginalized parameter constraints. The Ω_m uncertainty from the G³M analysis is $\sim 56\%$ of the cosmic shear result. The resulting shrinkage of the area within the 1- σ contour (Figure 9) shows that the information content of the G³M signal is greater, as also indicated by the raw S/N comparison (§4.2). We defer detailed comparison of our S_8 measurement with those from other studies to §5.

Since the galaxy bias parameters are degenerate with the amplitudes of the galaxy-galaxy and galaxy-mass power spectra ($P^{gg} \sim b^2 P_\delta$ and $P^{gm} \sim b P_\delta$), the tight correlations (degeneracies) of these parameter values with Ω_m and σ_8 are expected as shown in Figure 8. The marginalized b_1 (L1) and b_2 (L2) parameter constraints are $0.918^{+0.082}_{-0.134}$ and $1.161^{+0.127}_{-0.185}$, respectively. Since the error bars of the two parameters marginally overlap, the difference in their central values is only a weak indication of the possible bias evolution from $\langle z \rangle \sim 0.54$ to ~ 0.27 .

One useful consistency test between the galaxy-mass and the galaxy auto power spectra is to constrain galaxy biases independently from each method for a fixed cosmology. Figure 10 displays the results for the following two cases. In case 1, we fix Ω_m and σ_8 to our best-fit values and use only the galaxy clustering signal (GC-only). In case 2, we again fix Ω_m and σ_8 to our best-fit values, but this time use only the galaxy-mass power spectrum data (GGL-only). The results from these two cases are consistent with the ones that we ob-

¹⁶ This value is derived for the simulation using the cosmological parameters favored by the Planck CMB data. The exact value depends on the assumed cosmology. For example, when the simulation uses WMAP3 cosmological parameters, the best-fit value becomes $A_{\text{baryon}} = 3.43$.

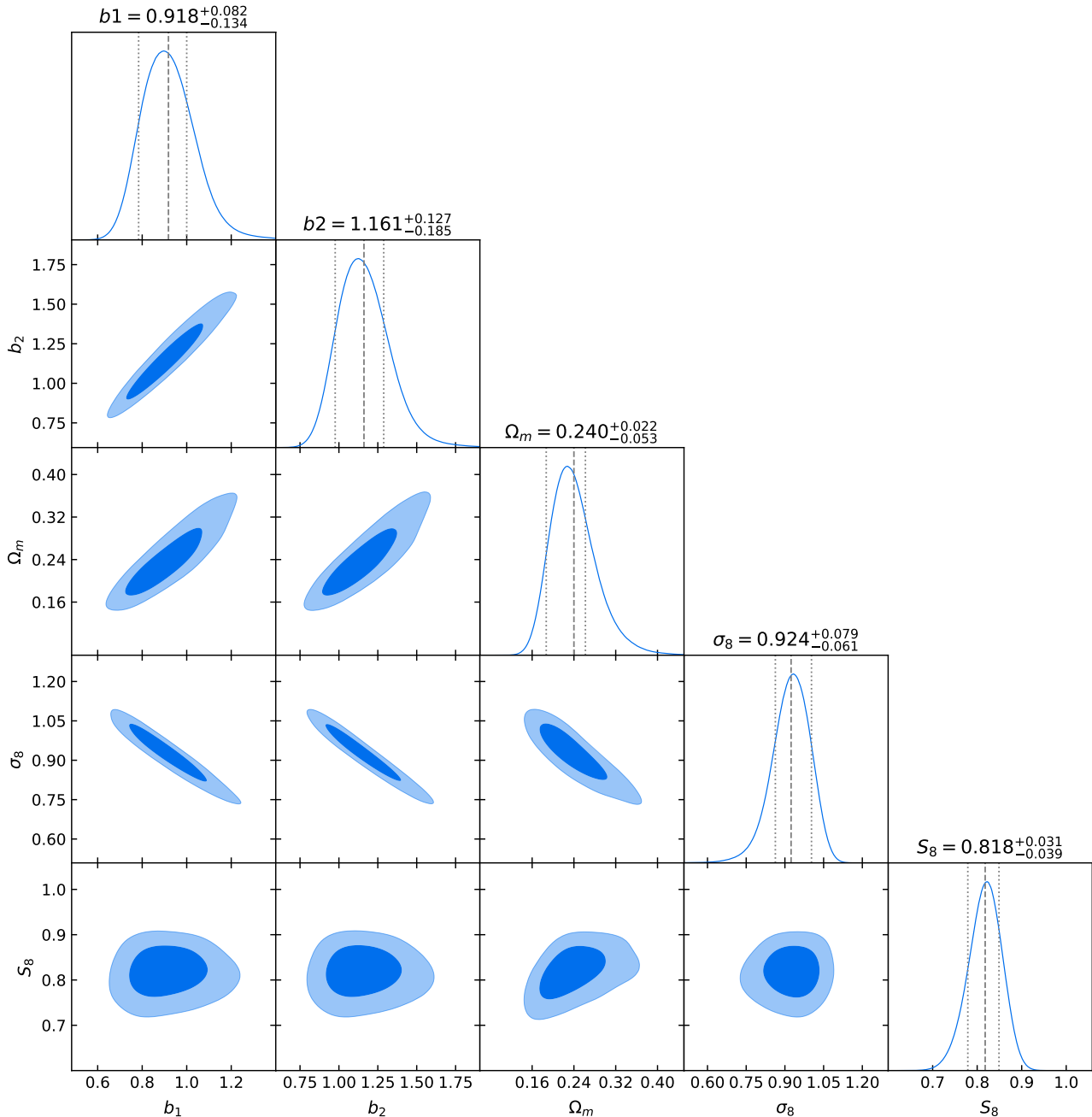


Figure 8. Constraints on b_1 , b_2 , Ω_m , and σ_8 estimated by our nested sampling for the flat Λ CDM model. Also displayed is the constraint on the derived parameter $S_8 \equiv \sigma_8(\Omega_m/0.3)^{0.5}$. The three parameters b_1 , b_2 , and Ω_m are positively correlated with one another while σ_8 is anti-correlated with these three parameters. S_8 shows no significant correlation with the other cosmological parameters.

tain after marginalizing over cosmological parameters. This test supports the internal consistency of the DLS data.

Beyond our baseline cosmology, we considered two one-parameter extension models to the flat Λ CDM cosmology, namely the non-flat Λ CDM and flat w CDM models. For the non-flat Λ CDM model, we let Ω_k vary within the interval $[-0.2, 0.2]$. We use a flat prior for the equation of state parameter $-1.5 < w < -0.5$ when w CDM is assumed. Of course, weak lensing alone does not constrain these two parameters. The goal of this experiment is to investigate how the Ω_m - σ_8 constraint changes as we assume these cosmologies. We display the results in Figure 11, which shows that the variation among the three models is only a few tens of per cent of the statistical errors. The marginalized Ω_m and

σ_8 values are summarized in Table 4.

5. DISCUSSION

5.1. Comparison of the DLS S_8 Measurement with Other Studies

Because of the well-known Ω_m - σ_8 degeneracy, the $S_8 \equiv \sigma_8(\Omega_m/0.3)^{0.5}$ value is a popular choice for comparing results from different surveys. In this paper, we also use this S_8 parameter to enable comparison with previous studies. However, it is important to remember that the comparison is fair only to the extent that the measurement (i.e., the exact shape of the degeneracy) favors this particular choice of the exponent 0.5.

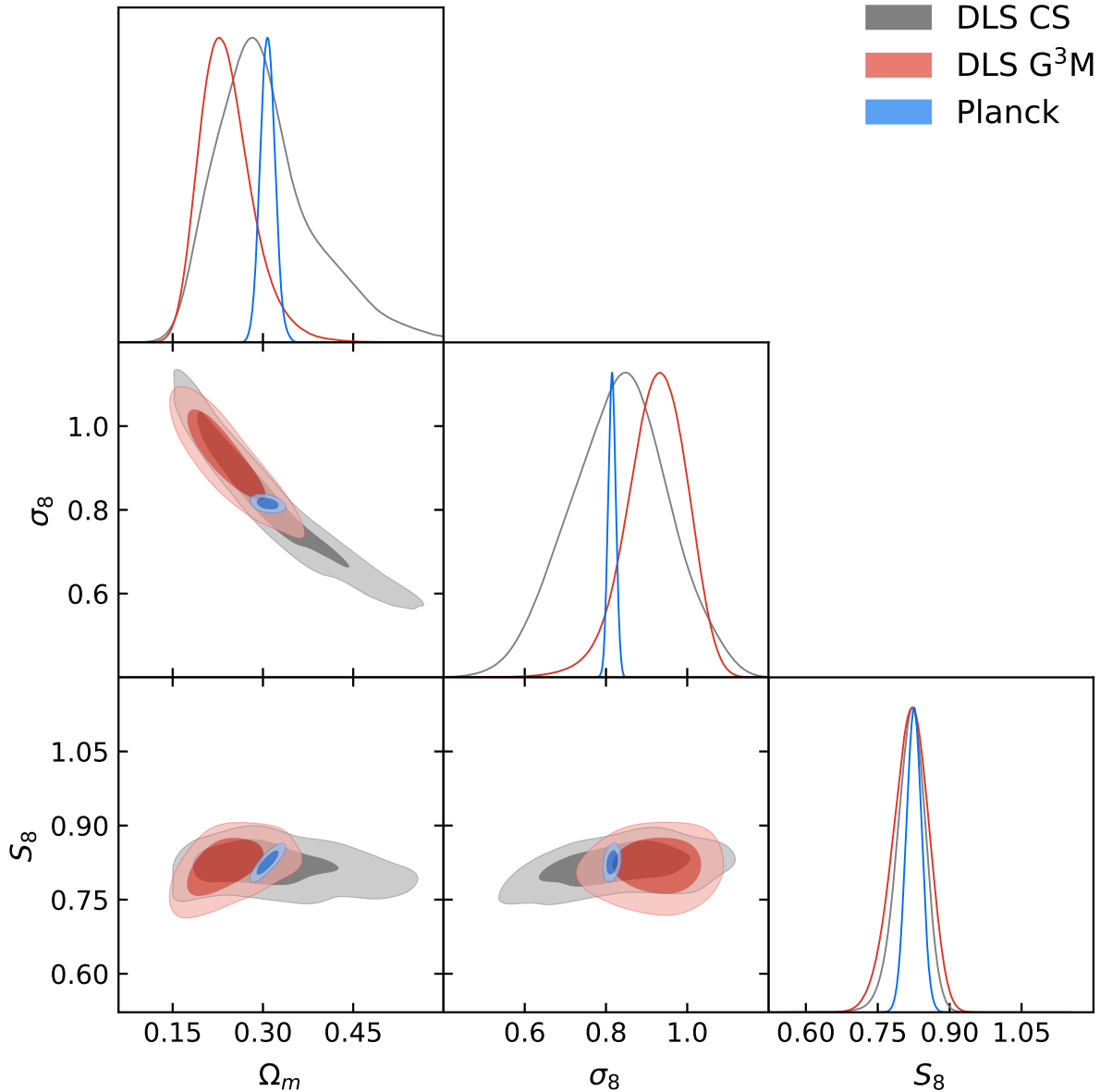


Figure 9. Constraints on σ_8 , Ω_m , and S_8 for a flat Λ CDM model from the G^3M method (red), from cosmic shear (grey), and from Planck2015 (blue). A smoothing kernel is applied. Two weak lensing analyses in DLS agree well and show no tension with Planck.

Table 4
Cosmological Parameter Constraints for Various Models

model	Ω_m	σ_8	S_8
Flat Λ CDM	$0.240^{+0.022}_{-0.053}$	$0.924^{+0.079}_{-0.061}$	$0.818^{+0.031}_{-0.039}$
Flat Λ CDM w/o baryon	$0.180^{+0.025}_{-0.031}$	$0.991^{+0.054}_{-0.058}$	$0.763^{+0.030}_{-0.040}$
w CDM	$0.232^{+0.030}_{-0.045}$	$0.957^{+0.074}_{-0.066}$	$0.833^{+0.044}_{-0.040}$
Non-flat Λ CDM	$0.230^{+0.023}_{-0.043}$	$0.936^{+0.067}_{-0.059}$	$0.812^{+0.051}_{-0.033}$

Note. — The selected models are a flat Λ CDM with/without baryonic feedback, a w CDM ($-1.5 < w < 1.5$), and a non-flat Λ CDM ($-0.2 < \Omega_k < 0.2$). We include AGN feedback and neutrino masses for both w CDM and non-flat Λ CDM.

The weak-lensing surveys that we use for comparison are

the CFHTLenS (Heymans et al. 2012; Joudaki et al. 2017a), DES Science Verification (Abbott et al. 2016), DES Year 1 (Abbott et al. 2017), and KiDS (Hildebrandt et al. 2017; van Uitert et al. 2018). The results from these surveys are compared with the DLS results in Figure 12. Also displayed in Figure 12 are the Planck constraints (Planck Collaboration et al. 2016, 2018, Planck temperature + low ℓ polarizations + lensing). The discrepancies between the S_8 values from some weak-lensing studies and the Planck CMB study and between the H_0 values from the direct measurements and the Planck CMB-inferred value (not shown) are often referred to as a “low- z vs. high- z tension”. If the tension is real, one may interpret the difference as indicating a need for some extensions of the standard Λ CDM model and/or revision of astrophysical models. For example, MacCrann et al. (2015) made an attempt to explain the tension between CFHTLenS and Planck with several additional parameters such as intrinsic alignment, AGN feedback, neutrino mass and neutrino

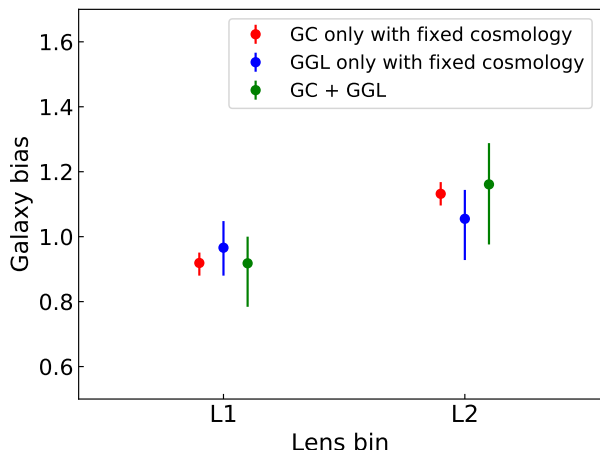


Figure 10. Galaxy bias measured for each lens bin under different conditions: galaxy clustering (P^{gg}) only with fixed cosmology (best-fitted Ω_m , σ_8), galaxy-galaxy lensing (P^{gm}) only with fixed cosmology, and both with free cosmological parameters. Independently measured galaxy biases are consistent with each other, validating the combined analysis of galaxy clustering and galaxy-galaxy lensing

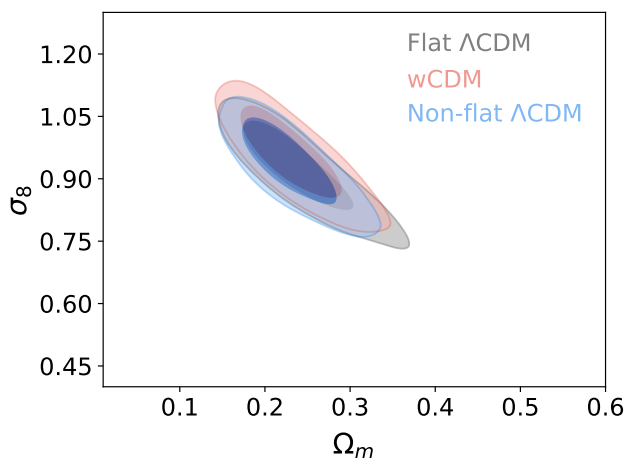


Figure 11. Constraints on σ_8 and Ω_m for the flat Λ CDM (grey), w CDM (red), and non-flat Λ CDM (blue) models. Little difference in parameter constraints is found among the three cosmological models.

species, etc. However, they found that none of the efforts could relieve the tension significantly. Joudaki et al. (2017b) showed the w CDM model is moderately preferred to relieve the tension in S_8 , but w CDM failed to relieve the tension in Hubble constant.

Among the results shown in Figure 12, the studies having a $\sim 2\sigma$ tension with the Planck results are the CFHTLenS (Heymans et al. 2012; Joudaki et al. 2017a), KiDS cosmic shear (Hildebrandt et al. 2017) and DES Year 1 3×2 pt (Abbott et al. 2017) whereas the DES SV cosmic shear (Abbott et al. 2016), KiDS+GAMA 3×2 pt power spectrum (van Uitert et al. 2018), and DLS studies do not show such a tension. The fact that some weak-lensing studies do not present any tension with the Planck CMB result may hint at the possibility that some surveys might have suffered from unknown systematics. For example, the two studies from KiDS produce somewhat different S_8 values. The KiDS tomographic cosmic shear analysis (Hildebrandt et al. 2017) leads

to $S_8 = 0.745 \pm 0.039$ whereas the KiDS study combining both cosmic shear and G^3M measurements (van Uitert et al. 2018) gives $S_8 = 0.800^{+0.029}_{-0.027}$. The statistical inconsistencies in KiDS are discussed in Efstathiou & Lemos (2018), who claim that it is too early to regard the tension as statistically meaningful.

5.2. Impacts of Assumed Cosmology on Parameter Estimation

In a few steps of our analysis, it is necessary for us to assume particular cosmological parameter values. They are the covariance matrix estimation (§4.2), the integral constraint computation in the galaxy auto-correlation measurement (§3.4), and the “tail” correction in correlation function evaluations (§4.1). Here we discuss the influence of the assumed cosmology.

The covariance matrix discussed in §4.2 consists of four parts: the shot noise, systematic error, mixed term, and sample variance. Because the sample variance is a function of cosmology, in principle the likelihood evaluation (Equation 25) needs to compute the covariance matrix in each sampling. In our study, we use the mock galaxy and shear catalogs from the FLASK package, whose resulting statistics follow log-normal distributions. Although this method is faster than the one that relies on N -body simulation data, it is still not feasible to implement the cosmology-dependent covariance. The cosmology-sensitivity in parameter estimation has been discussed in many studies (e.g., Eifler et al. 2009; Kilbinger et al. 2013; Jee et al. 2013; Dodelson & Schneider 2013), and the results are somewhat inconclusive. Perhaps, the issues somewhat depend on the method for covariance generation and the characteristics of the survey data.

We assess the impact of the cosmology dependence of the covariance matrix on our parameter estimation by repeating the analysis procedure using several covariance matrices generated at different cosmological parameters. From this limited test, we find that the results are mostly sensitive to the input σ_8 values. The central values do not differ much, showing no apparent correlation with the input σ_8 value, whereas the parameter errors certainly increase with σ_8 . For example, in two extreme cases, where we set the input σ_8 to 0.6 and 1.05, the difference in the central value of S_8 is ~ 0.006 whereas its error increases by $\sim 30\%$. Since our best-fit values are in good agreement with the input cosmology, we believe that the amount of bias in the parameter estimation and their errors (from not including cosmology-dependent covariance) is negligible.

With a similar method, we test the impact of the selected cosmology in the “tail” creation and IC evaluation. Since both the presence of the tail and the upshifting of the galaxy auto-correlation with IC values add to the amplitude of the power spectra at low ℓ ’s, we expect the central values of the estimated parameters to correlate with the input σ_8 value to some extent. Indeed, we find such a tendency in our experiment, although the difference is still smaller than the statistical errors. For example, the use of the input values $\sigma_8 = 0.6$ or 1.05 leads to a ~ 0.004 shift in S_8 ($\sim 12\%$ of the statistical error) compared to the result when the input value is $\sigma_8 = 0.83$.

5.3. Constraints on Baryonic Feedback Parameter and Model Selection

As shown in §4.3.4 and Figure 12, our introduction of the baryonic feedback parameter A_{baryon} leads to a higher value of S_8 than without it. This behavior is easy to understand because the net effect of the AGN feedback lowers the amplitude of the power spectrum. Although the marginalized probability of A_{baryon} is not constrained within the prior interval $2 < A_{baryon} < 4$ with the DLS data alone, it is a useful

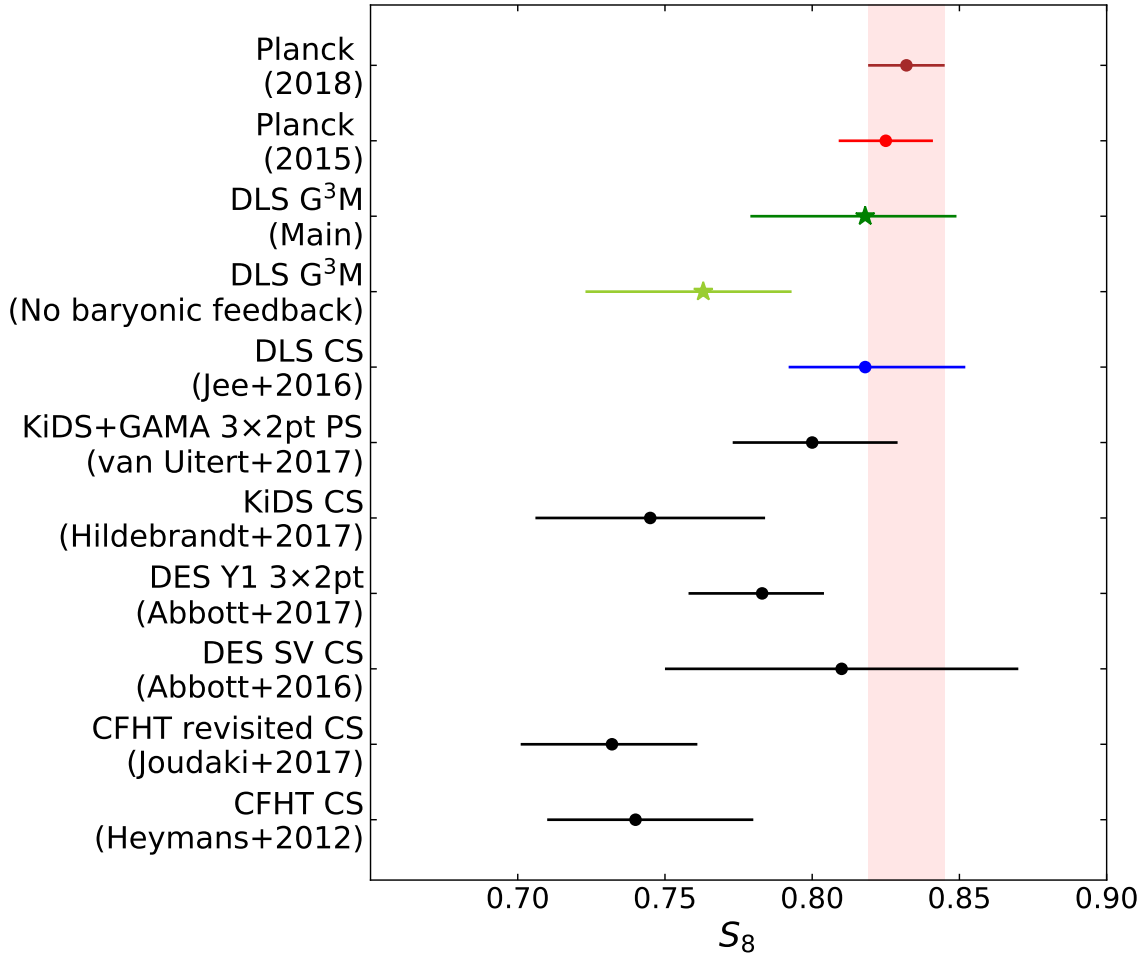


Figure 12. Comparison of S_8 values among different surveys: Planck2018 (brown), Planck2015 (red), DLS G³M with A_{baryon} marginalization (green), DLS G³M without A_{baryon} marginalization (light green), DLS cosmic shear (blue), KiDS, DES, and CFHT.

endeavor to constrain the parameter A_{baryon} combining our G³M measurement with external data.

We choose the Planck CMB data (Planck2015) because it provides independent, tight constraints on a number of cosmological parameters including Ω_m and σ_8 , which significantly increases the power to constrain A_{baryon} among other probes. We use the publicly available Planck likelihood code (Plik lite temperature + polarization)¹⁷ with a wider A_{baryon} prior range ($0.1 < A_{baryon} < 4$). As a result, we obtain $A_{baryon} = 1.07^{+0.29}_{-0.37}$ (Figure 13). This value is significantly smaller than the $A_{baryon} = 2.32$ value that corresponds to the baryonic effects with the AGN feedback in Mead et al. (2015). Note that this result is different from the conclusion of MacCrann et al. (2015). Their analysis with the combination of the CFHTLenS cosmic shear signal with the Planck CMB data does not show any preference for the power spectrum with the AGN feedback. Our result may hint at the possibility that actual AGN feedback might be stronger than the OWLS AGN feedback prescription. However, we cau-

tion that this interpretation is limited by the validity of this one-parameter representation (Eqn. 26) of the baryonic feedback effect for the power spectrum evaluation. As shown by Chisari et al. (2018), both the amount of suppression and the scale where the effect is most significant vary among different cosmological hydro-simulations. When we consider the three state-of-the-art simulations: Horizon-AGN, OWLS, and Illustris, the suppression from Illustris is most severe with the maximum $\sim 35\%$ reduction with respect to the dark matter-only power spectrum at $k \sim 6 h \text{ Mpc}^{-1}$. The maximum amount of suppression in OWLS is $\sim 30\%$ at $k \sim 10 h \text{ Mpc}^{-1}$. For the Horizon-AGN case, although the exact angular scale where the maximum suppression occurs is similar to that of OWLS, the amount of suppression is less than $\sim 15\%$.

It is possible that the baryonic feedback parameter may trade off with other cosmological parameters. Any strong degeneracy between parameters can lead to incorrect interpretation. For example, Harnois-Déraps et al. (2015) showed that the effect of neutrino mass is degenerate with baryonic feedback and thus cannot be ignored in cosmological parameter estimation. Since our measurement of A_{baryon} includes

¹⁷ <http://pla.esac.esa.int/pla/#cosmology>

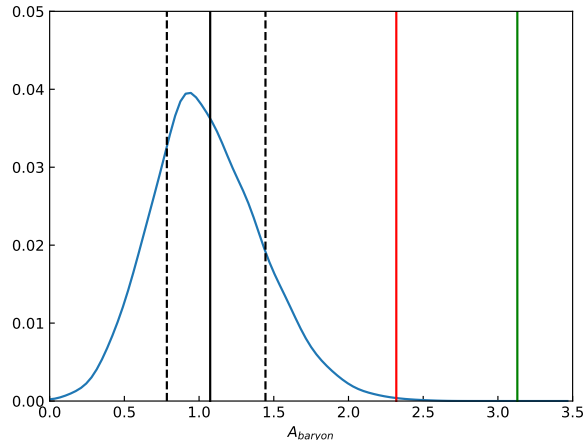


Figure 13. Constraint on the baryonic feedback parameter using the DLS and Planck2015 data. The blue solid curve is obtained after we apply a Gaussian kernel to smooth the marginalized one-dimensional histogram of A_{baryon} . The black solid line represents the mean whereas the dashed lines the $1\text{-}\sigma$ lower and upper limits. The red and green lines show the A_{baryon} values from Mead et al. (2015) corresponding to the AGN feedback and dark matter-only cases, respectively.

the marginalization over the sum of neutrino masses, this possibility is at least ruled out.

Together with the above A_{baryon} value constraint, another useful exercise is to test whether or not we can differentiate models with and without AGN feedback using the following Bayes factor:

$$BF = \frac{P(M_1|\mathbf{D})}{P(M_2|\mathbf{D})} \quad (28)$$

where $P(M_1|\mathbf{D})$ and $P(M_2|\mathbf{D})$ are the probabilities of the M_1 and M_2 models given data \mathbf{D} . Since $P(M|\mathbf{D}) = P(\mathbf{D}|M)P(M)$, evaluation of the above BF is performed using the Bayesian evidence $P(\mathbf{D}|M)$ with the assumption $P(M_1) = P(M_2)$. The computation of the evidence involves integrals of the likelihood in the parameter space θ over wide intervals:

$$P(\mathbf{D}|M) = \int P(\mathbf{D}|M, \theta)P(\theta|M)d\theta, \quad (29)$$

which is computationally more challenging than parameter estimation. We use the `multinest` package mentioned in §4.3.1 to carry out this integration. The evidence value also depends on whether or not we marginalize over neutrino masses and we measure them separately. Using the DLS G^3M data with (without) marginalizing over neutrino masses, we find the difference in the log evidences of the two models (dark matter-only vs. AGN feedback) to be ~ 2.0 (~ 3.1), which implies that the model with the inclusion of the baryonic effects with AGN feedback is preferred at a moderate level. This result is in slight contrast with the study of Joudaki et al. (2017a), who claim from the re-analysis of the CFHTLenS data that their cosmological parameter constraints do not show any preference between the two models. When we combine the current DLS data with the Planck CMB constraint, the difference in the log evidence becomes ~ 10.7 , strongly favoring the power spectrum with AGN feedback; in this latter case the evidence difference estimate is not affected by the inclusion of the neutrino mass marginalization.

6. SUMMARY AND CONCLUSIONS

We present cosmological parameter constraints by measuring galaxy-galaxy and galaxy-mass power spectra from the DLS. The power spectra are constructed using two lens bins at $\langle z \rangle = 0.27$ and 0.54 and two source bins at $\langle z \rangle = 0.64$ and 1.09 for the multipole range $\ell = 250 \sim 2000$. Our lens-source flip and B-mode tests do not reveal any significant systematic errors in photo- z and shear estimation. We address potential residual photo- z and shear calibration systematics by marginalizing over one shear calibration and four photo- z bias parameters in our cosmological parameter constraint. Also, we account for the power spectrum suppression due to both AGN feedback and neutrinos by employing the power spectrum model that includes the effects and marginalizing over the feedback and neutrino mass parameters.

The $S_8 = \sigma_8(\Omega_m/0.3)^{0.5}$ value is constrained to $S_8 = 0.818_{-0.039}^{+0.031}$. This value is in excellent agreement with our previous estimate from the DLS cosmic shear study. We expect that the cosmic shear-based S_8 value would increase somewhat when the baryonic feedback effect is included. Although the uncertainty of S_8 in the current study is slightly ($\sim 20\%$) larger than cosmic shear result, the $\Omega_m\text{-}\sigma_8$ degeneracy is reduced by $\sim 40\%$. Our result does not cause any tension with the value derived from the latest Planck measurement.

Our galaxy bias values are also well-constrained and show marginal evidence for redshift evolution; galaxies at higher redshift have larger bias. We examine the internal consistency by independently determining biases using the fixed, best-fit cosmology. The test shows that the results from both galaxy-galaxy and galaxy-mass power spectra are consistent with each other, although the signal for the possible redshift-evolution mostly comes from the galaxy-galaxy power spectrum.

The Bayesian evidence with the DLS-only case indicates that the power spectrum model with baryonic feedback is preferred at the moderate level. The combination of the DLS data with the Planck CMB measurements strongly favors the power spectrum with AGN feedback. We find that the best-fit S_8 value decreases by ~ 0.05 when we use a dark matter-only power spectrum. Considering the size of the parameter uncertainty (~ 0.04) and the angular scale of the power spectrum suppression, we believe that the difference is non-negligible.

Combining the current galaxy-galaxy and galaxy-mass power spectra with the Planck CMB data, we are able to constrain the baryonic feedback parameter to $A_{baryon} = 1.07_{-0.37}^{+0.29}$. This value is significantly smaller than the fiducial value $A_{baryon} = 2.32$, which is derived by matching the halo fit model power spectrum to the OWLS results with AGN feedback. Our A_{baryon} constraint may hint at the possibility that the recipe used in the OWLS simulation might have been weaker than actual AGN feedback. However, the interpretation is tentative until we verify the validity of this one-parameter representation of the baryonic feedback effect.

We thank Kyle Finner and Cris Sabiu for their careful reading of the manuscript and providing useful comments. M.J.J. acknowledges support for the current research from the National Research Foundation of Korea under the program 2017R1A2B2004644 and 2017R1A4A1015178.

REFERENCES

- Abbott, T., et al. 2016, Phys. Rev., D94, 022001
 Abbott, T. M. C., et al. 2017, arXiv:1708.01530
 Allen, S. W., Evrard, A. E., & Mantz, A. B. 2011, ARA&A, 49, 409
 Alonso, D., Bueno Belloso, A., Sánchez, F. J., García-Bellido, J., & Sánchez, E. 2014, MNRAS, 440, 10
 Beckwith, S. V. W., et al. 2006, AJ, 132, 1729
 Benítez, N., et al. 2004, ApJS, 150, 1
 Bennett, C. L., et al. 2003, ApJS, 148, 1
 Bridle, S., & King, L. 2007, New Journal of Physics, 9, 444

- Cacciato, M., van den Bosch, F. C., More, S., Mo, H., & Yang, X. 2013, MNRAS, 430, 767
- Catalan, P., Kamionkowski, M., & Blandford, R. D. 2001, MNRAS, 320, L7
- Chisari, N. E., et al. 2018, arXiv:1801.08559
- Choi, A., Tyson, J. A., Morrison, C. B., Jee, M. J., Schmidt, S. J., Margoniner, V. E., & Wittman, D. M. 2012, ApJ, 759, 101
- Coil, A. L., et al. 2011, ApJ, 741, 8
- Coles, P., & Jones, B. 1991, MNRAS, 248, 1
- Dodelson, S., & Schneider, M. D. 2013, Phys. Rev. D, 88, 063537
- Dubois, Y., et al. 2014, MNRAS, 444, 1453
- Efstathiou, G., & Lemos, P. 2018, MNRAS, 476, 151
- Eifler, T., Schneider, P., & Hartlap, J. 2009, A&A, 502, 721
- Eisenstein, D. J., & Hu, W. 1998, ApJ, 496, 605
- Eisenstein, D. J., et al. 2005, ApJ, 633, 560
- Feroz, F., Hobson, M. P., & Bridges, M. 2009, MNRAS, 398, 1601
- Gaztanaga, E., & Yokoyama, J. 1993, ApJ, 403, 450
- Geller, M. J., Dell'Antonio, I. P., Kurtz, M. J., Ramella, M., Fabricant, D. G., Caldwell, N., Tyson, J. A., & Wittman, D. 2005, ApJ, 635, L125
- Harnois-Déraps, J., van Waerbeke, L., Viola, M., & Heymans, C. 2015, MNRAS, 450, 1212
- Heymans, C., et al. 2013, MNRAS, 432, 2433
- Heymans, C., et al. 2012, MNRAS, 427, 146
- Hilbert, S., Hartlap, J., & Schneider, P. 2011, A&A, 536, A85
- Hildebrandt, H., et al. 2017, MNRAS, 465, 1454
- Hirata, C. M., & Seljak, U. 2004, Phys. Rev. D, 70, 063526
- Hubble, E. 1934, ApJ, 79, 8
- Huff, E. M., Eifler, T., Hirata, C. M., Mandelbaum, R., Schlegel, D., & Seljak, U. 2014, MNRAS, 440, 1322
- Jasche, J., Kitaura, F. S., Li, C., & Enßlin, T. A. 2010, MNRAS, 409, 355
- Jee, M. J., & Tyson, J. A. 2011, PASP, 123, 596
- Jee, M. J., Tyson, J. A., Hilbert, S., Schneider, M. D., Schmidt, S., & Wittman, D. 2016, ApJ, 824, 77
- Jee, M. J., Tyson, J. A., Schneider, M. D., Wittman, D., Schmidt, S., & Hilbert, S. 2013, ApJ, 765, 74
- Joachimi, B., Mandelbaum, R., Abdalla, F. B., & Bridle, S. L. 2011, A&A, 527, A26
- Joudaki, S., et al. 2017a, MNRAS, 465, 2033
- Joudaki, S., et al. 2017b, MNRAS, 471, 1259
- Kayo, I., Taruya, A., & Suto, Y. 2001, ApJ, 561, 22
- Kilbinger, M., et al. 2013, MNRAS, 430, 2200
- Kitching, T. D., Heavens, A. F., Taylor, A. N., Brown, M. L., Meisenheimer, K., Wolf, C., Gray, M. E., & Bacon, D. J. 2007, MNRAS, 376, 771
- Köhlinger, F., et al. 2016, MNRAS, 456, 1508
- Köhlinger, F., et al. 2017, MNRAS, 471, 4412
- Kwan, J., et al. 2017, MNRAS, 464, 4045
- Landy, S. D., & Szalay, A. S. 1993, ApJ, 412, 64
- Leauthaud, A., et al. 2017, MNRAS, 467, 3024
- MacCrann, N., Zuntz, J., Bridle, S., Jain, B., & Becker, M. R. 2015, MNRAS, 451, 2877
- Mandelbaum, R., et al. 2015, MNRAS, 450, 2963
- Mandelbaum, R., Slosar, A., Baldauf, T., Seljak, U., Hirata, C. M., Nakajima, R., Reyes, R., & Smith, R. E. 2013, MNRAS, 432, 1544
- Mead, A. J., Peacock, J. A., Heymans, C., Joudaki, S., & Heavens, A. F. 2015, MNRAS, 454, 1958
- Peebles, P. J. E. 1980, The large-scale structure of the universe
- Planck Collaboration, et al. 2016, Astron. Astrophys., 594, A13
- Planck Collaboration, et al.
- Riess, A. G., et al. 2018, ApJ, 855, 136
- Roche, N., & Eales, S. A. 1999, MNRAS, 307, 703
- Schaye, J., et al. 2010, MNRAS, 402, 1536
- Schmidt, S. J., & Thorman, P. 2013, MNRAS, 431, 2766
- Schneider, P., van Waerbeke, L., Kilbinger, M., & Mellier, Y. 2002, A&A, 396, 1
- Schrabback, T., et al. 2010, A&A, 516, A63
- Singh, S., Mandelbaum, R., Seljak, U., Slosar, A., & Vazquez Gonzalez, J. 2017, MNRAS, 471, 3827
- Skilling, J. 2006, Bayesian Anal., 1, 833
- Smith, R. E., et al. 2003, MNRAS, 341, 1311
- Springel, V., et al. 2018, MNRAS, 475, 676
- Suzuki, N., et al. 2012, ApJ, 746, 85
- Takahashi, R., Sato, M., Nishimichi, T., Taruya, A., & Oguri, M. 2012, ApJ, 761, 152
- Taylor, A. N., & Watts, P. I. R. 2000, MNRAS, 314, 92
- Troxel, M. A., et al. 2017, arXiv:1708.01538
- van Daalen, M. P., Schaye, J., Booth, C. M., & Dalla Vecchia, C. 2011, MNRAS, 415, 3649
- van Uitert, E., et al. 2018, MNRAS, 476, 4662
- Vogelsberger, M., et al. 2014, MNRAS, 444, 1518
- Wittman, D. 2009, ApJ, 700, L174
- Xavier, H. S., Abdalla, F. B., & Joachimi, B. 2016, MNRAS, 459, 3693
- Zhan, H. 2006, JCAP, 8, 008

APPENDIX

APPENDIX A. L1 AND L2 REDSHIFT DISTRIBUTION CALIBRATION

It is generally agreed that the photo- z bias of a galaxy population is reduced when one constructs the population's $p(z)$ by stacking $p(z)$ of individual galaxies rather than point estimates (e.g., Wittman 2009). A further reduction of the bias can be done through comparison of photo- z data with spectroscopic catalogs. For DLS, this photo- z calibration is possible for L1 and L2. In terms of both magnitude and redshift ranges, the PRIMUS catalog is nearly complete for both L1 and L2 whereas the SHELS catalog is complete for L1. Thus, we use only the PRIMUS catalog for L2 and both catalogs for L1. For L1 we have 5,647 and 1,749 matching galaxies from SHELS and PRIMUS, respectively. On the other hand, we find 2,488 spectroscopic objects for L2. We note that this kind of the $p(z)$ calibration is not feasible for S1 and S2 because of the incompleteness of the spectroscopic catalogs.

Figure 14 compares the population $p(z)$ constructed from the point-estimate photo- z 's, spec- z 's, and stacked $p(z)$ of individual galaxies. We use the Kernel Density Estimator (KDE) to obtain the smooth $p(z)$ curves of the point-estimate photo- z 's and spec- z 's. We find that the bias is non-negligible for L1. The mean redshift of the L1 population would be underestimated by $\sim 10\%$ if left uncorrected whereas the agreement between photo- z and spec- z is excellent for the L2 galaxies (the difference in the mean is less than 1%). The large discrepancy for the L1 population is caused by severe degeneracies for galaxies reported to be $z_b < 0.4$ by BPZ. The lack of a U filter in the DLS is known to be one of the main sources of the degeneracy in this redshift range. In this study, we address the issue by stretching the redshift range of the stacked $p(z)$ curve using Equation 27 so that the resulting mean matches the spectroscopic value. We find that this $p(z)$ calibration results in the reduction of S_8 by ~ 0.02 compared to the case without the calibration. The amount of the shift corresponds to $\sim 50\%$ of the statistical error.

Even after the above $p(z)$ calibration, the difference in the $p(z)$ shape still remains. Thus, we considered completely replacing the $p(z)$ with the spectroscopic $p(z)$ and found that our cosmological parameters virtually remain unchanged. Nevertheless, we think that this complete replacement lacks justification because the spectroscopic sample is only available to F2 and F5.

One powerful method to test the fidelity of this $p(z)$ calibration is to measure galaxy cross-correlation signals between L1 and L2 and compare them with the theoretical prediction based on these calibrated $p(z)$ curves. Figure 15 shows the remarkable agreement between the theoretical cross-correlation function and the measurement. Also displayed is the prediction based on the uncalibrated $p(z)$ curve, which is clearly offset from the measurement. The increase in the predicted cross-correlation is due to the enlarged overlap in $p(z)$ between L1 and L2. This cross-correlation test serves as a verification of our $p(z)$ calibration. We note that although one may consider using the cross-correlation measurements as additional constraints, in this study we only employ them for our $p(z)$ calibration verification.

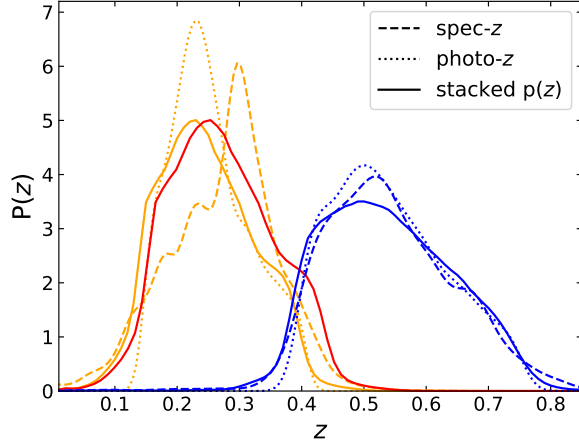


Figure 14. Calibration of the DLS photometric redshift distribution with spectroscopic data. We compare the population $p(z)$ distribution constructed from spec- z 's, point-estimate photo- z 's, and stacked $p(z)$ curves. We use orange and blue colors to represent the L1 and L2 populations, respectively. The bias is negligible for L2 whereas it is not for L1. The mean redshift of the L1 population would be underestimated by $\sim 10\%$ if left uncorrected. The red solid curve shows our correction made by stretching the $p(z)$ curve horizontally so that the resulting mean agrees with the one from the spec- z catalog. As noted in the text, this $p(z)$ calibration leads to the reduction of S_8 by ~ 0.02 , which is $\sim 50\%$ of the statistical error.

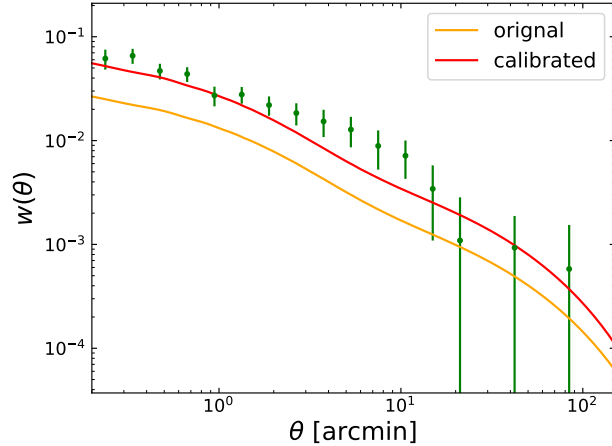


Figure 15. Galaxy-galaxy cross-correlation between L1 and L2. The green dots with error bars show the direct measurements. The amplitude should not be zero as shown because of the overlap in $p(z)$ between the two populations. The uncalibrated L1 $p(z)$ curve (orange solid line in Figure 14) does not sufficiently overlap with the $p(z)$ distribution of L2 and the predicted cross-correlation (orange) is significantly lower than the observation. Our $p(z)$ calibration (red) remarkably improves the agreement. When we predict the cross-correlation using the spec- z $p(z)$ (orange dashed line in Figure 14), the values are virtually identical to the results from the calibrated $p(z)$.

APPENDIX B. IMPACT OF RANDOM SIGNAL SUBTRACTION ON TANGENTIAL SHEAR MEASUREMENT

When tangential shears are measured, in principle, averaging over many lens-source galaxy pairs reduces/cancels additive shear biases. However, in practice, irregular sky coverage due to field boundaries and stellar masking regions hampers this bias reduction and increases field-to-field signal variations. The situation can be remedied by subtraction of tangential shears measured from randomly distributed (lens) points (Singh et al. 2017). We show the effect of this random signal subtraction in Figure 16. With this correction, the size of the errors decreases and also the central values shift as shown. The change is more noticeable at large angles. The DLS is composed of five fields (F1-F5) and thus biases introduced by different observational footprints cause the tangential shear measurements of different fields to deviate considerably from one another, which increases statistical errors when they are averaged. After the correction, the tangential shear measurements from different fields become more consistent with one another.

This correction is applied not only when we measure the tangential shear from the DLS but also when we estimate covariance from FLASK simulations. We apply the DLS star masking and the field boundaries to the simulated fields and subtract the signals measured from the pairs of random points and the simulated source galaxies. As tested in Singh et al. (2017), this provides a useful method to estimate an unbiased covariance taking account of field boundaries and star masking.

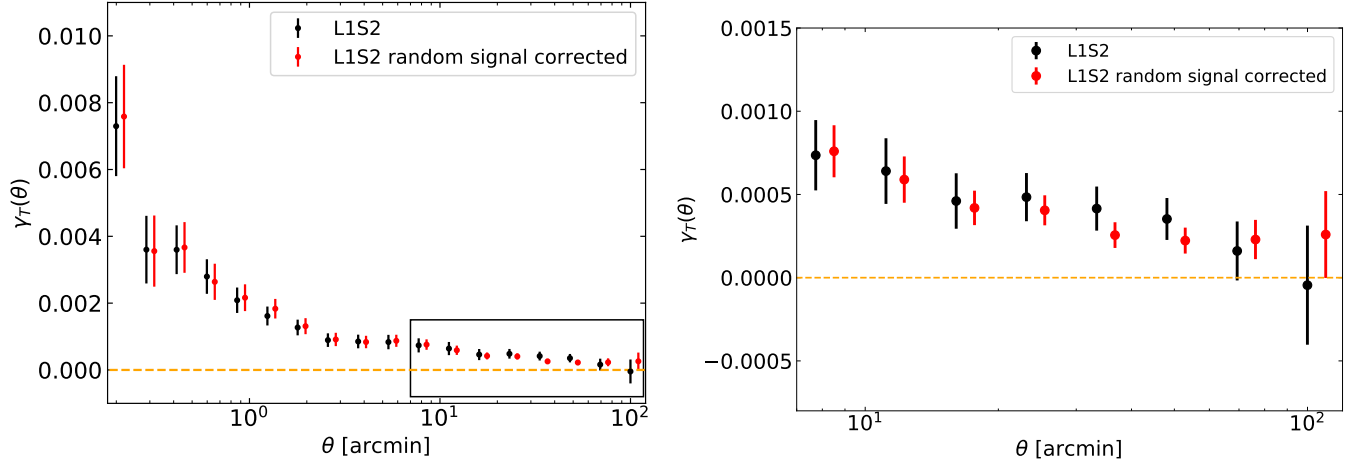


Figure 16. Tangential shear comparison between the cases with (red) and without (black) random signal subtraction. The displayed case is for the L1S2 pair. The right panel is a zoomed-in version showing the boxed region of the left panel. As shown, the random signal subtraction reduces both statistical and systematic errors caused by survey boundaries and star masking.

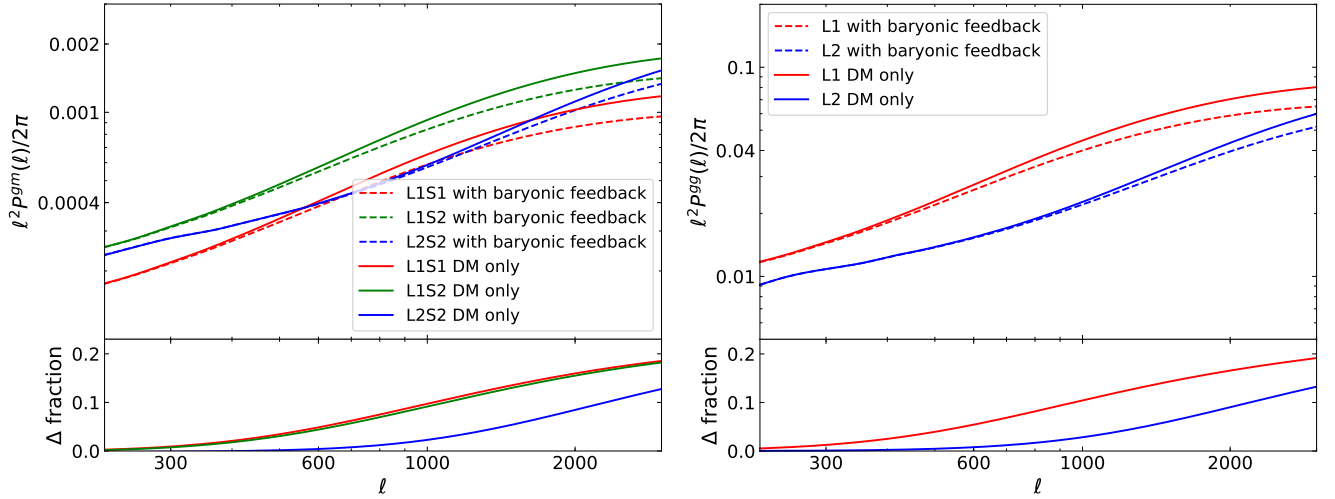


Figure 17. Comparison of galaxy-galaxy (P^{gg}) and galaxy-mass (P^{gm}) power spectra with (dashed) and without (solid) AGN feedback. The bottom panel shows the fractional difference between the two with respect to the dark matter-only model. We fix the cosmological parameters to our best-fit results. Following Mead et al. (2015), we use $A_{\text{baryon}} = 2.32$ and 3.13 for the cases with and without AGN feedback, respectively. The suppression of the power at large ℓ values is significant, reaching up to $\sim 18\%$ at $\ell \sim 2000$.

APPENDIX C. POWER SPECTRUM COMPARISON WITH/WITHOUT BARYONIC FEEDBACK

A common method to deal with unknown baryonic effects on the model power spectrum has been removal of signals on small scales, which results in significant loss of the survey S/N. In this paper, we choose to address the issue by using the Mead et al. (2015) power spectrum to control the degree of baryonic feedback using the single parameter A_{baryon} . In Figure 17, we show the P^{gg} and P^{gm} power spectrum shifts due to the baryonic effects including AGN feedback. We use $A_{\text{baryon}} = 2.32$ to represent the case of the baryonic effects with AGN feedback, which is the best-fit result to the OWLS simulation according to Mead et al. (2015); the dark matter-only case corresponds to $A_{\text{baryon}} = 3.13$. It is clear that the suppression of the power at large ℓ 's is significant and up to $\sim 18\%$ at $\ell \sim 2000$.

APPENDIX D. POWER SPECTRUM COMPARISON WITH/WITHOUT MASSIVE NEUTRINO

Similarly to baryonic feedback, massive neutrinos also suppress the power on small scales. That is, the baryonic feedback effect is degenerate with the effect played by massive neutrinos. Here we illustrate how much our P^{gg} and P^{gm} power spectra are affected by massive neutrinos. Figure 18 shows the impact of massive neutrinos on the galaxy-galaxy and galaxy-mass power spectra for the case $\Sigma_\nu m_\nu = 0.6$ eV, which approximately corresponds to the 95% upper limit constrained by Planck2015. The maximum departure from the dark matter-only case (without AGN feedback) is $\sim 3\%$, given the same matter power spectrum normalization σ_8 . Note that neutrinos in general suppress power on small scales. However, when we choose to normalize the power spectrum with neutrinos in such a way that the result gives the same σ_8 value from the case with zero neutrino mass, the resulting shift is both positive and negative depending on scales.

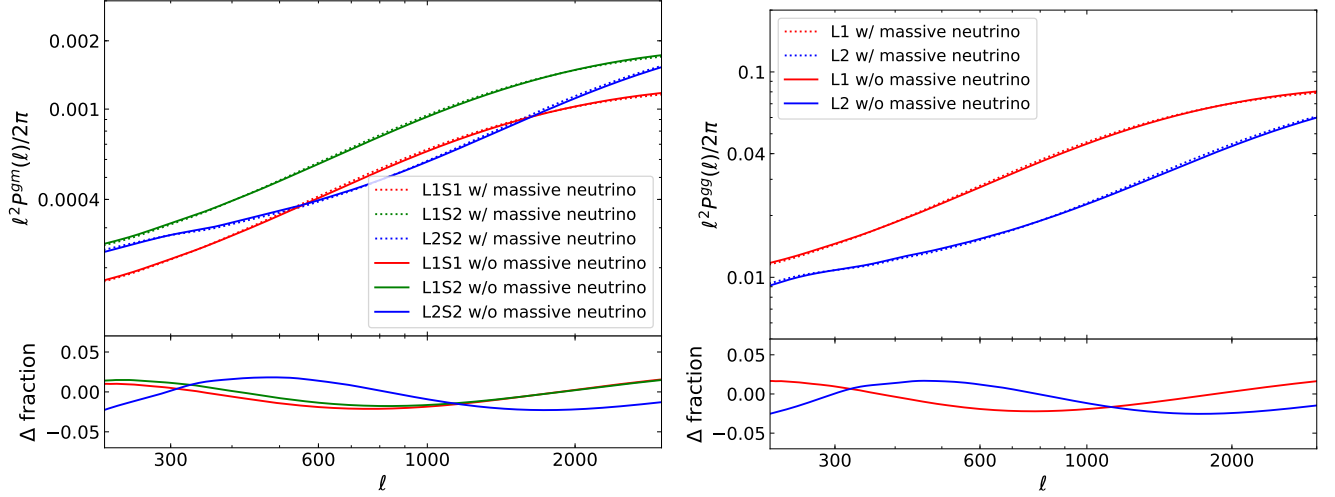


Figure 18. Comparison of galaxy-galaxy (P^{gg}) and galaxy-mass (P^{gm}) power spectra without (solid) and with (dotted) massive neutrinos ($\Sigma_\nu m_\nu = 0.6$ eV). The bottom panel shows the fractional difference with respect to the case without massive neutrinos. We fix the cosmological parameters to our best-fit results.